ROCK2 inhibition has a dual role in reducing ECM remodelling and cell growth, while impairing migration and invasion

Authors:

Daniel A. Reed[1,2], Anna E. Howell[1], Nadia Kuepper[1], Alice M. H. Tran[1], Astrid Magenau[1,2], Deborah S. Barkauskas[1], Max Nobis[1,2,3], Cecilia R. Chambers[1,2,4], Victoria Lee[1], Lily M. Channon[1], Jessie Zhu[1,2], Shona Ritchie[1,2], Janett Stoehr[1], Kaitlin Wylie[1,2], Julia Chen[1,2,5], Denise Attwater[1], Kate Harvey[1], Sunny Z. Wu[1,2,6], Kate Saw[1], Ruth J. Lyons[1], Anaiis Zaratzian[1], Michael Tayao[1], Andrew Da Silva[1], David Gallego-Ortega[7], Anthony J. Gill[1,8,9], Thomas R. Cox[1,2], Brooke A. Pereira[1,2], Kendelle J. Murphy[1,2], Jennifer P. Morton[10,11], Elgene Lim[1,2], Alex Swarbrick[1,2], Sandra O'Toole[1,2,12], Michael S. Samuel[13,14,15], C. Elizabeth Caldon[1,2], Alexandra Zanin-Zhorov[16], Paul Timpson[1,2] and David Herrmann[1,2,17].

[1]Cancer Ecosystems Program, Garvan Institute of Medical Research and The Kinghorn Cancer Centre, Darlinghurst, Sydney, New South Wales, Australia.

[2]School of Clinical Medicine, Faculty of Medicine and Health, University of New South Wales (UNSW), Kensington, Sydney, New South Wales, Australia.

[3]VIB-KU Leuven Center for Cancer Biology, Leuven, Belgium.

[4]IDIBELL Institut d'Investigació Biomèdica de Bellvitge, Barcelona, Spain.

[5]Department of Medical Oncology, St George Hospital, Sydney, New South Wales, Australia.

[6]Genentech Inc., South San Francisco, CA, USA.

[7]Single Cell Genomics Facility, School of Biomedical Engineering, Faculty of Engineering and IT, The University of Technology Sydney, Ultimo, NSW, 2007, Australia.

[8]NSW Health Pathology, Department of Anatomical Pathology, Royal North Shore Hospital, St Leonards, Sydney, New South Wales, Australia.

[9]Sydney Medical School, University of Sydney, Sydney, New South Wales, Australia.

[10]Cancer Research UK Scotland Institute, Glasgow, UK.

[11]School of Cancer Sciences, Wolfson Wohl Cancer Research Centre, University of Glasgow, Glasgow, UK.

[12]Royal Prince Alfred Hospital and NSW Health Pathology, School of Medical Sciences, University of Sydney, Sydney, NSW, Australia.

29 [13]Centre for Cancer Biology, an Alliance between SA Pathology and the University of South Australia,
30 Adelaide, Australia.

31 [14]Adelaide Medical School, Faculty of Health and Medical Sciences, University of Adelaide, Adelaide,
32 Australia.

33 [15]Basil Hetzel Institute for Translational Health Research, Woodville South, Adelaide, Australia.

34 [16]Graviton Bioscience Corporation, Graviton Bioscience B.V., Amsterdam, Netherlands.

35 [17]Lead contact. Correspondence to: d.herrmann@garvan.org.au

36 # Highlights

37 - Fibroblast-mediated remodelling of pre-existing and *de novo* synthesised extracellular matrix
38 is reduced upon ROCK2 specific targeting.
39 - ROCK2 inhibition impairs epithelial cancer cell growth and colony formation in 2D and 3D
40 contexts, while also limiting single-cell migration and cell survival upon fluid flow-induced
41 shear stress.
42 - ROCK2 targeting during fibroblast-mediated ECM remodelling is sufficient to disrupt collective
43 cell migration as well as 3D invasion into organotypic fibroblast-contracted collagen matrices.
44 - ROCK2 expression is up-regulated during breast cancer progression and high expression
45 correlates with poor patient outcome in triple-negative breast cancer.

Summary

The Rho-associated coiled-coil containing protein kinases 1/2 (ROCK1/2) are key signalling proteins involved in the regulation of the actin cytoskeleton and control a variety of cellular processes. This includes cell proliferation, stemness, cell migration and invasion as well as actomyosin contraction and extracellular matrix (ECM) remodelling. Due to a lack of ROCK2 specific inhibitors, previous pharmacological studies of ROCK function have relied on pan-ROCK1/2 inhibition. Here, we use the ROCK2 specific inhibitor, GV101, in the context of breast cancer (BC) models to uncouple the effects of ROCK2 pharmacological inhibition on both epithelial and stromal fibroblast cell populations. We demonstrate that ROCK2 inhibition with GV101 reduces fibroblast-mediated remodelling of pre-existing and *de novo* synthesised ECM resulting in a reduction in biomechanical stiffness, while also limiting epithelial cell growth in 2D and 3D settings. We also demonstrate that ROCK2 inhibition exposes epithelial cell vulnerability to fluid flow-induced shear stress. Furthermore, using 3D co-cultures we reveal that GV101 reduces single-cell migratory capacity, while the disruption of stromal ECM architecture is sufficient to impede collective cell migration and invasion. Finally, we assessed ROCK2 expression in human BC patient tumours revealing that ROCK2 expression is up-regulated during BC progression and that high ROCK2 expression correlates with poor patient outcome in the triple-negative subtype of BC. Together, these results demonstrate that ROCK2 specific inhibition disrupts key functions in both epithelial cell and stromal fibroblast compartments warranting further assessment of ROCK2 in highly proliferative, fibrotic or metastatic diseases, such as BC.

65 Keywords

66 ROCK2

67 Cell-ECM interactions

68 Cancer-associated fibroblasts

69 ECM remodelling

70 ECM stiffness

71 Epithelial cell biology

72 Cell migration and invasion dynamics

73 Breast cancer

74 Triple-negative breast cancer

Introduction

The extracellular environment delivers both mechanical and biochemical signals that influence cellular interactions with their surroundings, leading to alterations in various cellular functions during development, tissue homeostasis and disease progression. The Rho-associated coiled-coil containing protein kinases 1/2 (ROCK1/2) are central regulators of actin cytoskeletal processes, integrating multiple cellular processes that are crucial for both developmental and homeostatic physiology. Activation of ROCK predominantly occurs through binding of the small GTPase RhoA, a key signalling node facilitating outside-in-signalling from multiple extracellular inputs, resulting in a conformational change and subsequent relieving of auto-inhibitory interaction [1]. ROCK activation results in the phosphorylation of multiple downstream targets including myosin II regulatory light chain kinase (MLCK), the myosin binding subunit MYPT1 and LIM kinases, which can further regulate actin-binding proteins, such as cofilin [2]. This leads to the collective promotion of actin filament stabilisation and bundling, driving actomyosin contraction [3-5]. Due to its crucial role in actin cytoskeleton regulation, ROCK signalling is critical for a variety of cytoskeleton-dependent cellular processes including cell proliferation [6, 7], survival and apoptosis [8-10], migration and invasion [11-13], anchorage-independent growth [14-16], anoikis [17] and resistance to shear stress forces [18, 19]. Moreover, extracellular matrix (ECM) deposition and remodelling leading to the generation of a biomechanically stiff environment can be promoted further by ROCK activation [20, 21]. As a result, the ROCK signalling axis has been implicated in a variety of diseases and hence inhibition of ROCK has long been pursued as a possible therapeutic option in multiple pathologies [1, 22, 23].

ROCK1/2 are widely expressed in embryonic and adult tissues [24] and while the two proteins have many overlapping functions, they often exhibit tissue, cell or even subcellular specific roles [25]. Genetic studies have been critical in understanding the individual roles of both ROCK1 and ROCK2 in homeostatic and disease contexts, while pharmacological studies have been limited to the use of pan-ROCK1/2 inhibitors such as Fasudil and Y27632. We and others have shown that these ROCK1/2 inhibitors demonstrate promising proof-of-principle efficacy of ROCK inhibition in a variety of pre-clinical disease contexts, including cardiovascular disease [26], neurodegenerative disorders [27, 28], autoimmune disease [29, 30], idiopathic pulmonary fibrosis [31, 32] and various solid cancers [33-37]. However, the translation of these findings has been difficult due to the low specificity and tolerability of pan-ROCK1/2 inhibitors [38].

ROCK2 specific inhibitors therefore offer the promise of on-target ROCK2 inhibition while avoiding the negative side effects associated with previous pan ROCK1/2 inhibitors. For example, Belumosudil has shown promising results for the treatment of fibrotic diseases [39-41] and immunological disorders

108 [42-45], yet still exhibits off-target kinase inhibition [44, 46], limiting its evaluation on targeting the
109 ROCK2 signalling pathway specifically. Excitingly, a more potent ROCK2 inhibitor, GV101 (1000-fold
110 selective for the ROCK2 isoform over ROCK1) was recently shown to stall fibrosis in a mouse model of
111 non-alcoholic fatty liver disease [47]. However, the effects of ROCK2 inhibitors on basic cellular
112 function, such as cell proliferation, migration, invasion and ECM remodelling, have not yet been
113 assessed in other disease settings. This therefore warrants further investigation to uncover the effects
114 of ROCK2 inhibition on these key cellular processes.

115 Here we use triple-negative breast cancer (TNBC), a disease characterised by highly proliferative and
116 invasive epithelial cells as well as significant ECM deposition and remodelling [48, 49], as a model
117 system to decipher the effects of ROCK2 inhibition using GV101 on epithelial and stromal cell
118 populations in both murine and human-derived settings. We demonstrate that ROCK2 inhibition
119 reduces fibroblast-mediated remodelling of pre-existing and *de novo* synthesised collagen as well as
120 decreasing epithelial cell growth and colony formation in 2-dimensional (2D) contexts and under 3D
121 anchorage-independent growth settings. We further investigated the effects of ROCK2 inhibition on
122 epithelial cell migration on cell-derived matrices (CDMs) and show that GV101 reduces the single-cell
123 migratory capacity of epithelial cells, while disrupting the matrix production by fibroblast cells with
124 GV101 altered subsequent epithelial collective cell migration. We also reveal that ROCK2 inhibition
125 following fluid flow-induced shear stress enhances vulnerability to cell death. Moreover, we uncouple
126 the effects of epithelial *versus* stromal ROCK2 targeting by assessing epithelial cell invasion into 3D
127 fibroblast-contracted organotypic matrices, where ROCK2 inhibition to disrupt collagen remodelling
128 is sufficient to inhibit epithelial cell invasion. Finally, we provide evidence that ROCK2 may play an
129 important role in disease progression and survival in the triple-negative subtype of breast cancer,
130 suggesting that ROCK2 inhibition should be further investigated in this highly lethal disease.

131 # Results

132 ## ROCK2 inhibition with GV101 reduces fibroblast-mediated remodelling of pre-existing
133 and *de novo* ECM

134 The role of the ROCK signalling axis in ECM remodelling and stiffening has been well documented [6,
135 20, 33, 34]. Conversely, RhoA-ROCK signalling can also be activated by ECM tension and rigid
136 environments [20, 35]. This leads to further ECM and tissue stiffening, driving a feed-forward loop that
137 contributes to the pathogenesis of various diseases involving tissue fibrosis [50-54]. Here, we first
138 investigated how the ROCK2 specific inhibitor GV101 could modulate ECM remodelling in the setting
139 of TNBC, a highly fibrotic BC subtype [48]. One of the key cell types involved in ECM synthesis and
140 remodelling in tumours are cancer-associated fibroblasts (CAFs), which are present in mouse models
141 of the disease and human patients [55, 56]. In this study we utilised CAFs previously isolated from end-
142 stage tumours of the genetically engineered MMTV-PyMT mouse model of BC [35, 57] as well as CAFs
143 isolated from human TNBC patients [55, 58]. Both PyMT and human CAFs were shown to express
144 ROCK2 (Figure S1A) and its downstream target Cofilin [2, 47], which was de-phosphorylated upon
145 GV101 treatment (Figure S1B and C). This data indicates that we can target ROCK2 in the stromal TNBC
146 fibroblast compartment as previously achieved in the context of liver fibrosis [47].

147 To investigate the effects of ROCK2 inhibition *via* GV101 on CAF-mediated collagen contraction and
148 remodelling, we initially performed organotypic contraction assays, which provide a malleable
149 platform from which to assess key features of CAF-mediated contraction, remodelling and
150 biomechanics of pre-existing ECM [59]. Here, CAFs were embedded into acid-extracted fibrillar
151 collagen and allowed to contract and remodel the collagen matrix over a 12-day period, as previously
152 described (Figure 1A) [33, 60-63]. Treatment with either GV101 or Fasudil during collagen contraction
153 reduced the contractile properties of PyMT CAFs compared to vehicle control, as seen by a significant
154 increase in matrix size at day 12 (Figure 1B). Fasudil treatment resulted in an additional decrease in
155 contraction compared to GV101 (Figure 1B), showing that both ROCK2 specific and pan ROCK1/2
156 inhibitors can reduce ECM contraction. In order to assess the biomechanical properties of the
157 organotypic matrix, we performed unconfined compression analysis, as previously achieved [62, 63].
158 This showed that both GV101 and Fasudil treated matrices exhibited a significant reduction in
159 organotypic matrix stiffness (Young's modulus) compared to vehicle control (Figure 1D). Extracellular
160 tension and stiff environments can further promote ROCK signalling through RhoA activation, and
161 hence GV101 may be able to inhibit this feed-forward loop by reducing both ROCK2 signalling as well
162 as its concomitant activation from the environment.

163 We next employed multiphoton-based second harmonic generation (SHG) imaging and picrosirius red
164 staining to evaluate how GV101 affected the abundance and remodelling of fibrillar collagen. SHG
165 imaging of fibrillar collagen I content (Figure 1C, top panel, magenta and Movie S1) demonstrated a
166 significant decrease in SHG signal intensity in both GV101 and Fasudil treated matrices compared to
167 vehicle control (Figure 1E). Moreover, picrosirius red staining to assess total fibrillar collagen I/III
168 content (Figure 1C, middle panel) revealed a subtle, non-significant decrease in picrosirius red staining
169 coverage (Figure 1F). We also performed polarised light imaging of the picrosirius red stained matrices
170 to assess collagen birefringence where we observed a subtle decrease in total birefringence signal
171 (Figure 1G). Interestingly, analysis of green, yellow and red-orange birefringence signal (indicative of
172 low, intermediate and highly bundled collagen fibres respectively) showed a significant decrease in
173 red-orange birefringence signal (Figure S1D and G) upon GV101 treatment. This correlates to a
174 decrease in highly bundled collagen fibres following ROCK2 inhibition and suggesting that ROCK2 may
175 be required for the generation of mature collagen fibres in this setting. Treatment with Fasudil
176 reduced green, yellow and red-orange birefringence signal (Figure S1D to G, respectively), as well as
177 the total birefringence signal (Figure 1G), suggesting that pan ROCK1/2 inhibitors can limit early and
178 late remodelling of collagen/ECM. Collectively, these data show that GV101-mediated ROCK2
179 inhibition impairs CAF function on pre-existing ECM at several levels including CAF-mediated collagen
180 matrix remodelling, contraction and stiffening.

181 In order to corroborate our findings from mouse PyMT CAFs, we next assessed the effects of GV101
182 on human TNBC CAF function. As before, human TNBC CAFs [55, 58] were embedded into fibrillar
183 collagen for matrix contraction (Figure 1H). Similar to the murine model, human TNBC CAFs showed a
184 significantly decreased ability to contract the collagen matrix when treated with GV101 compared to
185 vehicle (Figure 1I). Interestingly, in this setting no significant differences in contraction were observed
186 when CAF matrices were treated with Fasudil compared to vehicle (Figure 1I). Assessment of the
187 biomechanical properties of these matrices similarly showed a significant decrease in organotypic
188 matrix stiffness upon GV101-mediated ROCK2 inhibition (Figure 1K). Multiphoton imaging showed a
189 decrease in SHG signal intensity indicative of lower fibrillar collagen I content in GV101-treated
190 matrices (Figure 1J, top panel, Figure 1L and Movie S2), while picrosirius red staining (Figure 1J, middle
191 panel) revealed a decrease in total fibrillar collagen I/III coverage in the matrices with GV101
192 treatment (Figure 1M). Moreover, polarised light birefringence imaging demonstrated a reduction in
193 total (Figure 1N), green (Figure S1H and I), yellow (Figure S1H and J) and red-orange (Figure S1H and
194 K) birefringence signal upon GV101 treatment, suggesting that ROCK2 inhibition in the human TNBC
195 CAF context affects all stages of collagen fibre maturation, bundling and crosslinking. Conversely,
196 Fasudil treatment only resulted in a significant decrease in matrix stiffness (Figure 1K) with a trend

197 towards decreased SHG (Figure 1L), picrosirius red coverage (Figure 1M) and birefringence signal
198 (Figure 1N, Figure S1H to K). Overall, these data using human TNBC CAFs align with the data obtained
199 in the murine PyMT CAF setting showing that GV101 can inhibit fibroblast-mediated collagen
200 remodelling, contraction and stiffness.

201 While the function of ROCK2 to facilitate the remodelling of pre-existing ECM has been characterised,
202 less is known about the effects of ROCK2 inhibition on the *de novo* production of ECM. In order to
203 assess this aspect of CAF biology in relation to ROCK2 inhibition, cell-derived matrix (CDM) assays were
204 employed as described previously [33, 62, 64-66]. Here CAFs are grown in a monolayer and then
205 treated with ascorbic acid to stimulate matrix production with concurrent ROCK2 or pan-ROCK1/2
206 inhibition [33, 62, 65] (Figure 2A). SHG imaging was then used to characterise *de novo* deposited ECM
207 (Figure 2B, top panel and Movie S3 and Movie S4). CDMs generated by PyMT CAFs treated with either
208 GV101 or Fasudil, showed a significant decrease in SHG signal intensity compared to vehicle control
209 indicative of a reduction in fibrillar collagen I abundance (Figure 2Ci). Furthermore, brightfield imaging
210 of picrosirius red stained CDMs confirmed a decrease in fibrillar collagen production across both
211 treatment groups compared to vehicle (Figure 2B, bottom panel and Figure 2Cii), corroborating that
212 GV101-mediated ROCK2 inhibition impairs the deposition and remodelling of *de novo* synthesised
213 fibrillar collagen. Similarly, in the human TNBC CAF setting we observe that GV101 reduced SHG signal
214 intensity and picrosirius red coverage to the same extent as Fasudil, as observed before in murine
215 CAFs (Figure 2D and E and Movie S5 and Movie S6). Collectively, this data demonstrates a requirement
216 for ROCK2 in CAF biology, in particular the contraction and remodelling of pre-existing collagen as well
217 as the deposition and remodelling of *de novo* synthesised ECM in both murine and human breast
218 cancer CAFs.

219

220 ROCK2 inhibition with GV101 reduces epithelial cell growth in 2D and 3D and sensitises
221 cells to fluid flow-induced shear stress

222 In addition to its role in stromal populations, ROCK signalling has also previously been identified to
223 promote pathways involved in cell growth and survival [7, 8, 10]. Here, we assessed ROCK2 inhibition
224 on these cellular functions utilising murine BC cells, isolated from end-stage tumours of the genetically
225 engineered MMTV-PyMT mouse model [57, 67], and the human TNBC cell line MDA-MB-231. Both cell
226 lines demonstrated ROCK2 expression (Figure S2A) and as shown before in CAFs (Figure S1), treatment
227 of both cell lines with GV101 showed a decrease in pCofilin (Figure S2B and C), demonstrating that
228 GV101 is able to reduce ROCK2 signalling in these cells. We first assessed the effects of GV101 on
229 baseline cell viability. Here, both murine PyMT and human MDA-MB-231 cells treated with GV101

230 showed a significant decrease in cell viability compared to vehicle control with only a subtle decrease
231 in cell viability observed using the pan-ROCK1/2 inhibitor Fasudil (Figure S2D and E) as previously
232 shown in other contexts [33, 36, 37].

233 Next, we aimed to assess the effect of ROCK2 inhibition on colony outgrowth from individual cells
234 using 2D colony formation assays (Figure 3A and B). Here, GV101 treatment significantly reduced the
235 colony forming capacity of PyMT cancer cells at all concentrations tested compared to vehicle (Figure
236 3Ai and ii). Similar growth inhibition effects were observed in the human MDA-MB-231 TNBC cell line
237 where GV101 treatment at all concentrations tested was sufficient to reduce colony outgrowth (Figure
238 3Bi and ii). We next investigated the effect of ROCK2 inhibition on 3D colony survival and outgrowth
239 under AIG conditions.[14, 16]. Here, single PyMT and MDA-MB-231 cancer cells were suspended in
240 agarose and incubated for 14 and 10 days, respectively, as previously described [33, 62]. Both PyMT
241 (Figure 3C) and MDA-MB-231 cells (Figure 3E) treated with GV101 showed a reduced ability to form
242 3D AIG clusters, as seen by a significant decrease in the number of clusters (Figure 3Di and Fi), as well
243 as a decrease in the size of colonies that are able to grow (Figure 3Dii and Fii), indicative of both a
244 reduction in 3D cell survival and proliferation, respectively. Collectively, these data demonstrate that
245 ROCK2 inhibition can affect colony outgrowth from individual cells under both 2D and 3D conditions.

246 In addition, biomechanical stress is well-known to induce ROCK signalling in cells [18-20], which can
247 protect cells from mechanical damage and subsequent cell death. We therefore next assessed the
248 effects of GV101-mediated ROCK2 inhibition on cell survival following fluid flow-induced shear stress
249 [33, 62, 67]. Here, we subjected cells to shear stress at a rate of 100 µL/s, as previously achieved
250 (Figure 3G) [33, 62, 67]. Following 20 cycles of shear stress, single cells were seeded to observe colony
251 outgrowth in the presence of GV101 or vehicle. Cell survival was assessed *via* live AnnexinV imaging
252 of apoptosis followed by segmentation of cells and AnnexinV signal to determine the proportion of
253 apoptotic cells (Figure S3A and Figure S3B). In PyMT cancer cells, shear stress alone did not increase
254 apoptosis (Figure 3H, compare DMSO P0 and P20), while the addition of GV101 after shear stress
255 exposure (P20) significantly increased apoptosis compared to vehicle (Figure 3H). Similarly, MDA-MB-
256 231 cells showed a non-significant increase in apoptosis following shear stress which again increased
257 with GV101 addition (Figure 3I), in line with the PyMT data. Overall, this suggests that ROCK2 is
258 important for cell survival following fluid flow-induced shear stress and that ROCK2 inhibition with
259 GV101 can expose cell vulnerability to apoptosis in this setting [68].

260

261 ## ROCK2 inhibition reduces single cell migratory dynamics

262 Another well characterised role of ROCK signalling is its function as a driver of cell migration through
263 regulation of the actin cytoskeleton and integration of cell-ECM or environment interactions [13]. This
264 has been demonstrated during developmental processes [69, 70] as well as in disease contexts such
265 as cancer, where co-opted ROCK signalling can promote cancer cell migration, invasion and metastasis
266 [11, 12, 33]. To assess the effects of GV101 on single-cell migration across an ECM substrate, we first
267 generated CDMs (Figure 4A) as described previously [33, 60, 63, 65, 66]. Following 7 days of matrix
268 deposition, CDMs were de-cellularised leaving the native ECM behind, onto which cancer cells were
269 then seeded (Figure 4A). Once adhered to the CDM, cells were treated with GV101 or vehicle and
270 single cell migration was tracked longitudinally over a 12-hour period, as previously achieved [62, 64,
271 65]. As PyMT cancer cells were found to not be highly migratory on a CDM (data not shown), single-
272 cell migration upon ROCK2 inhibition was assessed using the MDA-MB-231 cell line. Polar plots of
273 individual cell tracks over the 12-hour period showed that GV101 treatment profoundly impaired the
274 ability of cells to migrate on a CDM compared to vehicle (Figure 4B). Quantification of key cell
275 migration readouts further confirmed a significant decrease in average distance travelled, average
276 track displacement and maximum distance travelled over a 12-hour period for cells treated with
277 GV101 compared to vehicle (Figure 4Ci to iii, Movie S7). In addition, a significant decrease in the
278 migratory speed of these cells was also observed with GV101 treatment compared to vehicle (Figure
279 4Civ). Overall, this data demonstrates that ROCK2 is required for key locomotive processes of
280 individual cells on a CDM.

281

282 ## Stromal ROCK2 governs subsequent collective migration dynamics of epithelial cells

283 While our initial studies focussed on understanding the requirement for ROCK2 in isolated fibroblast
284 and epithelial cells, both cell populations co-exist *in vivo* where interactions between cancer cells and
285 the adjacent ECM create a reciprocal activation of ROCK signalling. Moreover, in addition to single cell
286 migration, cells can also move *via* collective migration, where the ECM can act as a guide to organise
287 cellular migration [71-74]. This process is reliant on both intracellular cell migratory signalling as well
288 as cell-cell and cell-ECM adhesions, all of which have been shown to be regulated by ROCK signalling.
289 To investigate the effects of ROCK2 inhibition with GV101 on collective cell migration and cell-ECM
290 interactions, migration assays were performed on CDMs with the aim of dissecting the contribution
291 of stromal *versus* epithelial ROCK2 inhibition on collective cell migration (Figure 5Ai) [62, 65, 74]. Here
292 PyMT cancer cells were utilised as MDA-MB-231 cells did not form highly organised collective
293 migration phenotypes (data not shown). Firstly, the effects of ROCK2 inhibition *via* GV101 on cells to

294 initiate cell-ECM contacts with the CDM after cell attachment was investigated. Here, we quantified
295 circularity as a surrogate for cell elongation and attachment to the CDM 6 hours post seeding (Figure
296 5Aii and Movie S8). Cells treated with GV101 exhibited an increased circularity compared to vehicle
297 (Figure 5Bi and ii), indicating a reduced capability to engage effective cell-ECM attachment upon
298 ROCK2 inhibition. Collective cell migration was then assessed *via* measurement of cell streaming
299 anisotropy following GV101 treatment, where a high anisotropy indicates highly organised migration
300 whereas a low anisotropy correlates with disorganised migration (Figure 5C) [33, 62, 63, 75]. Here we
301 observed a subtle decrease in organised cell migration when cells were treated during the migration
302 phase with GV101 compared to vehicle control (Figure 5Dii and Movie S8). Overall, these data indicate
303 that epithelial ROCK2 inhibition with GV101 significantly affects cancer cell attachment while only
304 subtly reducing the organisation of collective cell migration.

305 It is well appreciated that in addition to intracellular signalling driving cell migration, extracellular cues
306 from the environment can affect cancer cell migratory behaviour. For example, subtle changes in ECM
307 can be sufficient to disrupt co-ordinated cell migration [33, 62, 76]. Given that we demonstrated a
308 reduction in *de novo* ECM deposition and remodelling in CDM assays upon ROCK2 inhibition (Figure
309 2), we next assessed how GV101 primed CDMs, where GV101 was provided during the matrix
310 production phase, would affect the subsequent ability of epithelial cells to undergo collective
311 migration. Here, fibroblasts were primed with GV101 or vehicle during the CDM matrix deposition
312 phase followed by de-cellularisation to remove the fibroblasts and subsequent GV101 washout to
313 assess PyMT cancer cell streaming in the absence of GV101 (Figure 5E). Cells were allowed to grow on
314 the CDMs for 24 hours prior to assessing collective cell migration *via* anisotropy quantification. Here,
315 we observed a significant decrease in the organisation of cellular streaming on GV101 primed CDMs
316 compared to vehicle (Figure 5Fi and ii, Movie S9). Interestingly, this decrease in organised collective
317 cell migration on GV101 primed CDMs was more pronounced than when GV101 was provided to
318 inhibit epithelial ROCK2 during the migration phase, highlighting a dominant role for the ECM
319 substrate in guiding collective cell migration. Overall, this data demonstrates that while epithelial
320 ROCK2 inhibition with GV101 perturbs cancer cell-ECM attachment, collective cell migration dynamics
321 is predominantly disrupted when *de novo* ECM deposition and remodelling is altered with GV101
322 treatment of ECM-producing fibroblasts.

323

Uncoupling epithelial *versus* stromal roles of ROCK2 during cancer cell invasion into 3D organotypic matrices

To further dissect the role of ROCK2 in the stromal *versus* epithelial compartment, we next used a 3D organotypic invasion assay, where cancer cells interact with and directionally invade into a fibroblast-contracted collagen matrix. Here, fibroblasts were embedded into a collagen matrix and allowed to contract the matrix over 12 days as described previously (Figure 1A) [33, 57, 60-63, 77-79]. Following contraction, MDA-MB-231 cancer cells were seeded on top of the fibroblast-contracted collagen matrices (Figure 6A). After 3 days of cell attachment and growth, the 3D organotypic cultures were placed on a metal grid to create an air-liquid interface producing a chemotactic gradient towards which the cancer cells were allowed to invade for 14 days (Figure 6A) [59, 63, 67, 79, 80]. Here, we aimed to uncouple the effects of stromal ROCK2 targeting with GV101 on creating an invasion-permissive environment by treating the CAFs during the contraction phase (early priming treatment) *versus* the effects of GV101 on epithelial ROCK2 function during cancer cell invasion (late invasion treatment) or in a continuous manner (chronic treatment, Figure 6A) as previously achieved [33, 62].

Importantly, we observed that in the control setting MDA-MB-231 cells readily invaded into the collagen matrix (Figure 6B) and this was not significantly altered upon late invasion treatment *via* epithelial ROCK2 inhibition with GV101 compared to vehicle (Figure 6B and C). Interestingly, in the early priming treatment setting we observed a significant decrease in cancer cell invasion when we targeted stromal ROCK2 during matrix contraction (Figure 6B and C). Moreover, in line with previous studies [33, 62], continuous or chronic treatment by targeting both stromal and epithelial ROCK2 decreased cancer cell invasion to a similar level as early priming, suggesting that the disruption of stromal ECM remodelling *via* GV101 alone is sufficient to decrease subsequent cancer cell invasion. This data further supports our previous results on collective cell migration (Figure 5) where modulation of the ECM *via* stromal ROCK2 targeting with GV101 was sufficient to alter subsequent collective cell migration dynamics. Collectively, we uncouple how targeting epithelial and stromal ROCK2 govern cell movement with a role for epithelial ROCK2 in individual cell migration whereas stromal ROCK2 directs subsequent collective cell migration and invasion.

ROCK2 expression increases during disease progression and correlates with poorer patient survival in TNBC cohorts

This study has demonstrated that ROCK2 inhibition with GV101 is able to reduce fibroblast-mediated remodelling of pre-existing and *de novo* synthesised collagen fibres. In addition, cell growth, proliferation and survival as well as cancer cell migration and invasion dynamics were also impaired

357 upon GV101 treatment. Here we have utilised models of BC to systematically investigate the
358 interactions between stromal and epithelial cells and their adjacent ECM due to the highly fibrotic,
359 proliferative and invasive nature of this disease. ROCK inhibition has long been anticipated as a
360 potential therapeutic target in a variety of cancer types, including BC, but efficacy and safety of
361 previous generation ROCK inhibitors has hampered clinical translation [5]. The findings from this study
362 suggest that ROCK2 inhibition may be able to impair cell proliferation, survival and invasion as well as
363 reduce fibrosis in BC models. We therefore aimed to investigate the role of the ROCK2 isoform
364 specifically in human BC patient cohorts. Analysis of both the METABRIC and TCGA BC cohorts revealed
365 that high ROCK2 mRNA expression significantly correlated with poorer patient median survival, (Figure
366 7A and Bi). Interestingly, we observed in TCGA data that the level of ROCK2 mRNA expression was also
367 significantly increased in the highly fibrotic and invasive TNBC subtype compared to other BC subtypes
368 combined (Figure 7Bii), suggesting that ROCK2 could play a role in TNBC disease progression and
369 survival.

370 We next interrogated ROCK2 protein expression *via* immunohistochemistry (IHC) in two independent
371 human BC TMA cohorts. Firstly, the Garvan/RPA Breast Progression Series was used to assess ROCK2
372 protein expression over disease progression. Staining and analysis of the Garvan/RPA Breast
373 Progression Series (Figure 7C) revealed that staining coverage was significantly increased at each stage
374 of disease from healthy (normal) breast tissue to Ductal Carcinoma In Situ (DCIS) and again from DCIS
375 to Invasive Ductal Carcinoma (IDCa, Figure 7Di). Mean and maximum staining intensity was also
376 increased, from normal breast tissue to DCIS (Figure 7Dii). Furthermore, a significant increase in the
377 average maximum intensity of the staining from normal tissue over DCIS to IDCa was observed (Figure
378 7Dii). Together this data shows that ROCK2 protein expression is significantly increased during BC
379 disease progression.

380 Secondly the RPA/CRGH TNBC cohort was used to assess ROCK2 protein expression in relation to
381 patient outcome in a TNBC-specific setting (Figure 7E). This revealed that high staining coverage
382 significantly correlated with poorer patient survival (Figure 7Fi). Similarly, we observed a decrease in
383 median survival for those patients with high staining intensity (Figure 7Fii). Moreover, combined
384 assessment of the staining coverage and intensity scores showed a significant decrease in median
385 survival for patients with high ROCK2 expression compared to those with low ROCK2 expression
386 (Figure 7Fiii). This data supports the mRNA data and overall indicates that high ROCK2 expression in
387 human TNBC patients correlates with poorer patient survival. Therefore, ROCK2 may represent a novel
388 target in TNBC warranting further interrogation of ROCK2 specific inhibitors in this disease context.

389

390 ## Discussion

391 The ROCK signalling axis has been well characterised in a variety of cellular processes including
392 actomyosin contraction, cell proliferation, apoptosis and migration as well as tissue-level processes
393 including ECM synthesis and remodelling [1, 6, 13]. As a result, dysregulation of this pathway has been
394 implicated in multiple diseases including but not limited to autoimmune, cardiovascular and fibrotic
395 diseases as well as solid cancers [5, 10, 22]. Inhibition of ROCK has been long suggested as a possible
396 therapy for these diseases due to the multi-faceted roles of ROCK signalling. For example, in cancers
397 that exhibit highly fibrotic signatures, such as pancreatic cancer and TNBC, ROCK inhibition was shown
398 to act as a dual targeting strategy reducing stromal fibrosis and stiffness to improve therapy delivery
399 and efficacy as well as directly limiting cancer cell proliferation and invasiveness [33, 54, 81]. These
400 earlier studies have been limited to the use of pan-ROCK1/2 inhibitors, which often exhibit undesired
401 side effects and toxicity. The generation of ROCK2 specific inhibitors with preferable safety profiles,
402 such as Belumosudil, has enabled assessment of ROCK2 inhibition, which was successfully translated
403 into humans for the treatment of chronic graft *versus* host disease [45, 82]. Most recently, GV101,
404 which has 1000-fold more selectivity for ROCK2 over ROCK1, was reported to stall fibrosis in a mouse
405 model of non-alcoholic fatty liver disease with increased efficacy over Belumosudil [47]. Here, we
406 assessed the effects of GV101-mediated ROCK2 inhibition on both stromal and epithelial cell biology
407 of BC. This study utilised TNBC as a model of a highly fibrotic, proliferative and invasive subtype of BC
408 to investigate the effects of ROCK2 inhibition with GV101 on key cellular processes in both stromal
409 and epithelial cell populations.

410 ECM synthesis and remodelling is often a defining feature of fibrotic diseases and has also been
411 implicated in various solid cancers, such as TNBC. The ROCK1/2 signalling axis plays a crucial role in
412 the remodelling and stiffening of the ECM through its control of actomyosin contraction [20, 34]. Here
413 we show that ROCK2 inhibition with GV101 reduces fibroblast-mediated collagen remodelling of pre-
414 existing collagen in organotypic matrices and of *de novo* synthesised collagen in CDM assays.

415 In addition to the regulation of ECM remodelling through actomyosin contraction, the ROCK signalling
416 axis has also been shown to regulate other cytoskeleton-dependent processes including cell
417 proliferation and survival [10, 83]; however, there is conflicting evidence as to the involvement of
418 ROCK1/2 in these processes depending on cell type. In non-small cell lung carcinoma deletion of both
419 ROCK1 and 2 was required to suppress cell proliferation [10], while in hepatocellular carcinoma and
420 neuroblastoma decreased ROCK2 expression alone was sufficient to reduce proliferation [36, 37].
421 Here, we demonstrate that in the setting of TNBC, ROCK2 inhibition reduces baseline cell viability as
422 well as colony outgrowth from individual cells in a 2D and 3D setting, again highlighting the context-

423 dependent or disease-specific role of this signalling axis. Furthermore, upon cell detachment from the
424 ECM, altered integrin signalling has been shown to activate ROCK2 resulting in cytoskeletal
425 rearrangements preventing anoikic cell death, a key feature of cancer cells allowing them to survive
426 in the absence of cell-substrate interaction under AIG conditions [14, 84]. In our study, inhibition of
427 ROCK2 with GV101 under AIG conditions resulted in a significantly reduced ability of cancer cells to
428 survive and grow out into colonies [33, 85]. Moreover, we also demonstrate that GV101 sensitises
429 cells to apoptosis following biomechanical stress, which is known to induce cell response *via* multiple
430 cytoskeletal rearrangements [68, 86]. Overall, these data highlight a role for ROCK2 in cell proliferation
431 and survival as well as in response to cell stressors such as AIG and fluid flow-induced shear stress
432 conditions.

433 In this study we also aimed to uncouple the effects of both epithelial and stromal cell ROCK2 inhibition
434 on subsequent cancer cell migration and directional invasion. We first investigated both single cell and
435 collective cell migration dynamics on CDMs upon ROCK2 inhibition, which provide readouts of cell
436 migratory capacity and also cell-ECM adhesion interactions. The ROCK signalling axis governs both
437 processes through its activation by upstream kinases, such as RhoA and Focal Adhesion Kinase (FAK)
438 from ECM-mediated input, as well as its downstream regulation of the actin cytoskeleton. In this study
439 we demonstrated that ROCK2 inhibition with GV101 reduces both single cell migratory distance and
440 speed. In the context of collective cell migration, epithelial ROCK2 inhibition with GV101 reduced
441 initial cell-ECM attachment, elongation and spreading. Interestingly, collective migration dynamics on
442 a CDM were only subtly altered following epithelial GV101 treatment, whereas manipulation of the
443 matrix on which the cells were seeded, *via* GV101 inhibition in fibroblasts during the ECM deposition
444 phase, resulted in a profound reduction of organised cell streaming. Importantly, this was superior to
445 epithelial ROCK2 inhibition alone. In addition, we demonstrated that GV101 disrupted the deposition
446 and remodelling of *de novo* synthesised ECM in a CDM setting and these results highlight that, in
447 particular stromal ROCK2 inhibition, has the capacity to alter subsequent collective cell migration
448 dynamics by modulating the extrinsic cell-ECM adhesions. Interestingly, manipulation of the stromal
449 ECM environment has also been observed to affect collective cell migration in other contexts, for
450 example FAK inhibition during CDM production affects collective pancreatic cancer cell migration
451 predominantly through cell extrinsic mechanisms [62].

452 Our results from CDM assays were further corroborated in a 3D context of directional cell invasion
453 into collagen matrices, where manipulation of fibroblast-mediated ECM remodelling *via* stromal
454 ROCK2 inhibition with GV101 was also sufficient and superior over epithelial ROCK2 inhibition to
455 reduce subsequent cancer cell invasion. Given the considerable effects that epithelial ROCK2 inhibition
456 has on reducing both cell growth and cell migration, the lack of efficacy in reducing cell invasion during

457 the late invasion treatment was surprising with only early stromal priming treatment reducing
458 invasion. However, this has also been observed with pan-ROCK1/2 inhibition in other contexts. For
459 example, in pancreatic cancer, pan-ROCK1/2 inhibition with Fasudil in the stromal compartment
460 during fibroblast-mediated matrix remodelling was sufficient to impair subsequent cancer cell
461 invasion into 3D organotypic invasion assays, to a greater extent than treatment of epithelial ROCK1/2
462 during the invasion phase [33]. Similar effects were observed upon FAK inhibition, where stromal FAK
463 inhibition reduced epithelial cell invasion [62]. Furthermore, the biomechanical properties of the
464 surrounding environment have been demonstrated to influence cancer cell invasion dynamics.
465 Inhibition of lysyl oxidase (LOX), a collagen-crosslinking enzyme, during collagen matrix remodelling
466 reduced matrix stiffness and subsequent cancer cell invasion [61]. In our study, we found that
467 inhibiting stromal ROCK2 with GV101 during matrix contraction reduced the matrix stiffness and these
468 biomechanical changes in the matrix are likely to contribute to the decreased cancer cell invasion
469 observed. Overall, this work demonstrates the impact of cell-ECM outside-in signalling on cancer cell
470 invasion and how manipulation of the surrounding ECM has effects on cell migratory and invasion
471 dynamics, which could be utilised to reduce cell motility in highly invasive cancers, such as BC.

472 The ROCK signalling pathway has been implicated in a number of solid cancers where high ROCK2
473 mRNA and protein expression has been correlated with more aggressive disease and poorer patient
474 survival [34, 87-91]. ROCK1/2 has also been found to be associated with BC metastasis with higher
475 levels of ROCK1/2 mRNA found in metastatic sites when compared to matched primary tumours [92].
476 Most recently it has been shown that ROCK1/2 protein expression and phosphorylation of its
477 downstream target, MYPT1, is increased in IDCa compared to normal/hyperplastic breast tissue [21]
478 overall highlighting ROCK signalling as potential target. Here, we assessed ROCK2 specifically in
479 relation to human BC disease showing that ROCK2 expression is increased during BC progression and
480 that high ROCK2 expression correlates with poor patient outcomes in TNBC, the most lethal subtype
481 of BC. Given the highly invasive and fibrotic nature of this disease, therapeutic interventions that
482 target both epithelial and stromal cell populations, such as ROCK2 inhibitors may be a therapeutic
483 option in this disease. However, given the highly context-dependent nature of ROCK2 signalling more
484 studies are needed to investigate ROCK2 inhibitors in disease-specific settings.

485 Overall, this study has set out to examine and uncouple the effects of ROCK2 inhibition *via* GV101 on
486 stromal and epithelial cellular function in isolated and co-culture models. Our findings demonstrate
487 that inhibition of stromal ROCK2 with GV101 can reduce the ECM deposition and remodelling ability
488 of stromal cells, while epithelial ROCK2 inhibition decreased cancer cell proliferation and survival.
489 Furthermore, we have demonstrated that disrupting stromal ECM deposition and remodelling *via*
490 stromal ROCK2 inhibition is sufficient to decrease subsequent collective cancer cell migration and

491 invasion. Finally, we also reveal that high ROCK2 expression correlates with poor patient outcomes in
492 the TNBC subtype of BC. Given these data we suggest that ROCK2 inhibitors should be further explored
493 in the context of other fibrotic diseases and solid cancers. In line with this, ROCK2 inhibition may
494 provide a dual targeting strategy to reduce both the fibrotic environment as well as decrease cancer
495 cell proliferation, warranting further assessment of this signalling node in BC.

Resource availability

Lead contact

Further information and requests for resources and reagents should be directed to and will be fulfilled by the lead contact, David Herrmann (d.herrmann@garvan.org.au).

Materials availability

All materials generated in this study will be available upon reasonable request from the lead contact.

Data and code availability

All information required to reanalyse the data reported in this study is available from the lead contact upon reasonable request.

507 # Acknowledgements

508 This study was supported by the following facilities at the Garvan Institute of Medical Research:
509 Australian BioResource (ABR), Biological Testing Facility (BTF), Garvan Molecular Genetics (GMG),
510 Tissue Culture Facility under Ruth Lyons, the Garvan Imaging Platform under Dr Deborah Barkauskas,
511 and the Garvan Histopathology and Biospecimen Facility under Anaiis Zaratzian. Some imaging was
512 performed at the UNSW Katharina Gaus Light Microscopy Facility. We also would like to thank the
513 staff of the ACRF INCITe Centre under co-leadership of T. G. Phan and P. Timpson. We would also like
514 to thank our consumers (E. Jurd, V. Killen, J. Mumford and D. Goulburn OAM) for their valuable input
515 regarding this work. Schematics were created with BioRender.com.

516 This study was supported by the National Health and Medical Research Council (NHMRC: 1136974,
517 1158590, 1160022, 1188208, 2000937, 2010330, 2012837, 2016930, 2018440, 2028766), US
518 Department of Defense Breast Cancer Research Program (BC210277), Cancer Council (RG 23-11, RG
519 19-09, RG 21-12, and RG 23-07), Cancer Institute NSW (CINSW; ECF012, ECF011, ECF1309, ECF1384,
520 CDF1071, CDF1173, CDF1167, and TPG2100), Cancer Australia (2021412), Tour de Cure (RSP-509-
521 FY2023), St. Vincent's Clinic Foundation, an Australian Cancer Research Foundation (ACRF)
522 infrastructure grant (INCITe Centre), Estée Lauder Award and Suttons family and Len Ainsworth
523 foundation philanthropy. P.T. was supported by a National Health and Medical Research Council
524 (NHMRC) Fellowship (1136974 and 2016930) and a Len Ainsworth Fellowship. T.R.C. was supported
525 by an NHMRC Investigator award (2033065) and Career Development Fellowship (1158590) and
526 CCNSW (24-06). K.W. was supported by an Australian Government Research Training Scholarship. A.S.
527 (2018440) was supported by a NHMRC Investigator Fellowships. M.N. (ECF012), K.J.M. (ECF1384),
528 B.A.P. (ECF1309) and D.H. (ECF011), and were supported by a CINSW Early Career Research
529 Fellowship. J.Z. was supported by a UNSW SPHERE Cancer CAG PhD scholarship. M.T. was supported
530 by a White Walker Cancer Research PhD scholarship. S.R. was supported by a UNSW International PhD
531 scholarship. M.S.S. was supported by an Australian Breast Cancer Research Fellowship from The
532 Hospital Research Foundation. D.A.R. and C.R.C. were supported by a Baxter Family Postgraduate
533 scholarship an Australian Government Research Training Scholarship.

Author contributions

Investigation, validation, and formal analysis: All authors. **Conceptualisation and funding acquisition:** D.A.R., M.N., K.J.M., B.A.P., D.G.-O., A.J.G., S.O'T., A.S., T.R.C., E.L., M.S.S., C.E.C., A.Z-Z., P.T. and D.H. **Writing, editing, and visualisation:** D.A.R., P.T. and D.H.

538 ## Declaration of interests

539 P.T. and D.H. receive reagents from Équilibre Biopharmaceuticals and Graviton Biosciences (GV101
540 provided free of charge). P.T. receives reagents from Kadmon Inc., InxMed (consultant) Redx Pharma,
541 and Amplia Therapeutics. Under a licensing agreement between Amplia Therapeutics and Garvan
542 Institute of Medical Research, K.J.M., P.T. (consultant) and D.H. are entitled to milestone payments.

543 # STAR Methods

544 ## Experimental models and study participant details

545 ### Statistical analysis

546 Unless otherwise stated, p-values were determined using an Unpaired t test for comparisons between
547 two groups or an Ordinary One-way ANOVA with Tukey's multiple comparison for comparisons
548 between three or more groups. For normalised data a One sample t test was used. For survival analysis
549 Kaplan-Meier survival curves were analysed using a log-rank (Mantel-Cox) test. All statistical analysis
550 was performed using GraphPad Prism (GraphPad Software Inc., CA, USA) with statistical significance
551 defined as ns = $p \geq 0.05$, * = $p < 0.05$, ** = $p < 0.01$, *** = $p < 0.001$, **** = $p < 0.0001$.

552 ## Human ethics

553 All research involving TMA biospecimens and associated data was covered by the Royal Prince Alfred
554 Hospital Human Ethics Review Committee Approval (X14-0241) with all patient data supplied in a
555 deidentified format.

556 ## Cell culture

557 PyMT 20065 cancer cells, herein referred to as PyMT cancer cells, previously generated by Dr Karen
558 Blyth at the CRUK Beatson Institute (Glasgow, UK) [67], were maintained in DMEM (Dulbecco's
559 modified Eagle medium, Gibco) supplemented with 10% Fetal Bovine Serum (FBS), 1%
560 penicillin/streptomycin (P/S), 5µg/mL insulin, 10ng/mL epidermal growth factor (EGF) and 10ng/mL
561 Cholera Toxin A. PyMT CAFs, previously isolated from end-stage MMTV-PyMT tumours [35] were
562 kindly provided by the lab of Dr Fernando Calvo lab and were maintained in DMEM supplemented
563 with 10% FBS, 1% P/S, and 1x Insulin-Transferrin-Selenium (ITS-G, Gibco). MDA-MB-231 cells and
564 Telomerase-immortalised fibroblasts (TIFs) [59] were maintained in DMEM supplemented with 10%
565 FBS and 1% P/S. Cells were maintained at 37°C and 5% CO_2 in a HeraCell 160i CO_2/O_2 incubator. Cell
566 lines were tested for mycoplasma and confirmed to be negative. Primary human TNBC patient CAFs,
567 obtained from Professors Elgene Lim and Alex Swarbrick at the Garvan Institute of Medical Research,
568 were maintained in alpha modified Eagle's media (αMEM) supplemented with 20% FBS and 1x
569 Antibiotic/Antimycotic (AB/AM, Gibco) in collagen coated flasks. For collagen coating, flasks were
570 incubated in 2mg/mL rat tail extracted collagen at 37°C for 2 hours. Following incubation flasks were
571 washed twice with phosphate-buffered saline (PBS) and then incubated in growth media for one hour.
572 Cells were maintained at 37°C, 5% O_2 and 5% CO_2 in a HeraCell 160i CO_2/O_2 incubator. All *in vitro*
573 experiments were carried out in the growth media stated above, unless stated otherwise.

574

575 ## Method details

576 ### Collagen extraction

577 Collagen I was isolated from rat tails as previously described [59]. Briefly, frozen rat tails were thawed
578 in 80% ethanol and collagen tendons removed from the tail using tweezers. Extracted tendons were
579 solubilised in 1.5L of 0.5M acetic acid (Fisher Chemicals) at 4°C for 48 hours with constant stirring using
580 a magnetic stirrer. Following solubilisation the mixture was filtered through a moist gauze to remove
581 any insolubilised tendons or sheath. Collagen I was then precipitated with 10% (w/v) NaCl at 4°C using
582 a magnetic stirrer until a homogenous solution was achieved (approximately 6-8 hours). The solution
583 was then centrifuged at 10,000 RPM for 30 minutes at 4°C to isolate precipitated collagen. Pelleted
584 collagen precipitate was then dissolved in 0.25M acetic acid at a 1:1 ratio for 24 hours at 4°C using a
585 magnetic stirrer. The collagen I solution was then dialysed in 17.4mM acetic acid for 3 days with acetic
586 acid solution being replaced every 12 hours. Following dialysis the mixture was centrifuged at 14,000
587 RPM at 4°C for 90 minutes to remove any debris. Collagen concentration was measured using the
588 Sircol™ Soluble Collagen Assay Kit (Biocolour) and was made up to a final solution of 2mg/mL in
589 17.4mM acetic acid prior to use.

590 ### Organotypic contraction assay

591 Organotypic contraction assays were performed as previously described [33, 57, 59, 61-63]. Rat tail
592 extracted collagen I dissolved in acetic acid at a concentration of 2 mg/mL was neutralised with 0.22M
593 sodium hydroxide with MEM 10x (Gibco). The neutralised collagen was kept on ice to prevent
594 polymerisation. CAFs were prepared in FBS and then added to neutralised collagen I solution, 2.5mL
595 of CAF/Collagen mixture was added to each well of a tissue culture (TC) treated plastic 6-well plate
596 (Corning) for a final concentration of $3.5x10^5$ PyMT CAFs or $2.5x10^4$ TNBC human CAFs per well.
597 Collagen/CAF matrices were placed at 37°C, 5% CO_2 until solidified. The solidified collagen matrices
598 were detached from the plate using a sterilised glass stripette, following addition of 5mL of
599 appropriate growth media containing 5µM GV101, 5µM Fasudil or DMSO control. Matrix contraction
600 took place over a 12-day period with drug containing media being replaced every 3 days along with
601 the scanning of plates using a HP Flatbed Scanner (Hewlett Packard) to assess matrix size during
602 contraction. Following 12 days of contraction matrices were fixed in 10% neutral buffered formalin for
603 histopathology processing. Matrix size was quantified using ImageJ (National Institute of Health (NIH),
604 USA) with three matrices analysed per condition for three independent repeats.

605 ### Unconfined compression analysis

606 Unconfined compression analysis was performed on organotypic matrices using a TA Instruments
607 Dynamic Hybrid Rheometer (DHR-3, TA Instruments), in line with previously published work [61, 93].

608 Hole-punch biopsies with a diameter of 8mm were taken from organotypic collagen contraction
609 matrices following 12 days of CAF mediated collagen contraction. Biopsies were placed between
610 80mm parallel plate geometries and a constant linear compression rate of 10µm/s was applied with
611 axial force and gap width being measured every one second. Data was analysed by creating a
612 stress/strain curve from axial force and gap measurements and the Young's modulus was determined
613 from the linear region of the stress/strain curve with three matrices analysed per condition for three
614 independent repeats.

615 Cell-derived matrix deposition assay

616 Cell-derived matrices (CDMs) were generated as previously published [65, 66]. PyMT CAFs ($6x10^4$
617 cells/well) or human TNBC CAFs ($2x10^5$ cells/well) were seeded in a TC treated plastic 24-well plate.
618 After 24 hours, confluent monolayers of CAFs were treated with 1mL of media containing 50µg
619 ascorbic acid (Sigma) to stimulate matrix production. Fresh ascorbic acid was added directly to wells
620 on days two and six with a complete media, drug and ascorbic refresh on day 4. Following one week
621 of matrix production matrices were fixed in 10% neutral buffered formalin for 24 hours followed by
622 70% ethanol for 24 hours before being imaged for SHG and subsequent picrosirius red staining.

623 Cell viability assay

624 PyMT 20065 cells ($5x10^2$ cells/well) or MDA-MB-231 cells ($4x10^4$ cells/well) were trypsinised with 0.5%
625 Trypsin-EDTA (Gibco) and then seeded in TC treated plastic 96-well plates (Corning) in appropriate
626 growth media. Following 16 hours of adhesion cells were treated with 1, 3, 5µM GV101, 5µM Fasudil
627 or DMSO control. Following 5 days of treatment cell viability was read out using an AlamarBlue™ Cell
628 Viability Reagent Kit (ThermoFisher). Briefly 10uL of AlamarBlue reagent was added to wells containing
629 200µL of media and absorbance was read out on a FLUOstar® Omega Microplate reader (BMG
630 Labtech) at an excitation of 544nm and emission of 590nm following 3.5 hours (PyMT 20065) or 5
631 hours (MDA-MB-231) of incubation. Cell viability was assessed in five wells per condition for three
632 independent repeats.

633 Colony formation assay

634 Cells were trypsinised with 0.5% Trypsin-EDTA (Gibco) then filtered sequentially through 100µm,
635 70µm and 40µm filters to obtain single cell suspensions. Cells were seeded at 500 cells/well (PyMT
636 20065) or $1.0x10^3$ cells/well (MDA-MB-231) in TC treated plastic 6-well plates (Corning). Following cell
637 attachment for 16 hours, cells were treated with 1, 3 or 5µM GV101 or DMSO control in appropriate
638 growth media. For PyMT cells, cells were fixed on day four and for MDA-MB-231 cells were fixed on
639 Day 14 by placing plates on ice and fixing with ice-cold 100% methanol for 20 minutes. Following
640 fixation wells were washed twice with PBS (Gibco) followed by staining with 0.5% crystal violet (Merck)

641 solution for 4 hours. Following staining wells were washed in water until excess crystal violet stain was
642 removed and then dried upside down overnight. Colony coverage assessed using ImageJ (NIH) in three
643 wells per condition for three independent repeats.

644 Anchorage-Independent Growth Assays

645 AIG assays were performed from a modified published protocol [62, 67]. Preparations of 10% and 3%
646 (w/v) low melting point agarose (SeaPlaque Agarose, Lonza) in H_2O was autoclaved at least 24 hours
647 prior to assay commencement. On the day of set-up both concentrations of agarose were microwaved
648 briefly and warmed in a water bath at 42ºC until molten. The 1% agarose solution was prepared by
649 diluting the autoclaved 10% solution in the appropriate phenol red free media. A bottom layer of 1%
650 agarose was made by adding 500µL of 1% agarose to the bottom of a TC treated plastic 24-well plate
651 and allowed to solidify at room temperature for one hour. Cells were trypsinised with 0.5% Trypsin-
652 EDTA (Gibco) then filtered sequentially through 100µm, 70µm and 40µm filters to obtain single cell
653 suspensions. The 0.3% molten agarose was combined at a 2:1 ratio with media containing
654 resuspended single cell solutions and 750µL of that final solution was added to 1% agarose base layer
655 for a final concentration of $1.0x10^4$ cells/well (PyMT 20065) or $5.0x10^3$ cells/well (MDA-MB-231).
656 Following 45 minutes incubation at room temperature 750µL of the appropriate phenol red free media
657 was added with GV101 or DMSO control for final concentrations of 1, 3 and 5µM GV101. PyMT 20065
658 cells were grown in AIG conditions for 14 days and MDA-MB-231 cells for 10 days. Following
659 completion of the assay individual AIG clusters were imaged using a DM4000 Leica microscope (Leica
660 Biosystems, 10 clusters/well) to assess average cluster size. To assess total number of clusters 10µL of
661 QuickDip II dye (Fronine Laboratory Supplies) was added to each well and following 24 hours of
662 incubation whole well pictures were acquired using a Leica MZ12.5 microscope (Leica Biosystems).
663 Average colony size was quantified in QuPath [94] via manual annotation and colony number
664 quantified in ImageJ. AIG colony formation was assessed in four wells per condition for three individual
665 repeats.

666 Flow-induced Shear Stress Assays

667 Flow-induced shear stress was performed as previously described [33, 62, 95]. PyMT or MDA-MB-231
668 cancer cells were trypsinised and filtered through a 70µm filter to a single cell suspension at a
669 concentration of $5x10^5$ cells/mL in appropriate growth media. Cells were exposed to 20 rounds of
670 shear stress through a 30-gauge needle at a constant flow rate of 100µl/s. After exposure to shear
671 stress $2x10^3$ cells were seeded in a 96 well plate with Incucyte® Annexin V Red dye (Sartorius) and
672 imaged on the Incucyte S3 live cell analysis instrument (Sartorius). For analysis cells were segmented
673 using the Cyto3 model in Cellpose and mask created to quantify cell coverage in ImageJ. Masks of

674 Annexin V were also generated in ImageJ and Annexin positive are was calculate from a ratio of
675 Annexin V positive area divided by total cell coverage, with 9 ROIs per well for 3 wells analysed per
676 condition for three independent repeats.

677 Single-Cell Migration Assays

678 Single-cell migration assays were performed from a modified protocol as previously published [62].
679 CDMs were generated as above with Telomerase-immortalised fibroblasts (TIFs). Following matrix
680 production TIF-derived matrices were denuded via incubation in extraction buffer (20nm NH_4OH, 0.5%
681 Triton X-100, 1% Sodium Deoxycholate in PBS) for 3 minutes. Following cell removal matrices were
682 carefully washed twice in PBS containing calcium and magnesium (1mM $CaCl_2$ and 1mM $MgSO_4$) and
683 incubated in 10ug/mL DNase I (Roche) in PBS containing calcium and magnesium at 37°C, 5% CO_2 for
684 30 minutes. Matrices were then washed twice in PBS containing calcium and magnesium before
685 incubation in appropriate cell culture medium. MDA-MB-231 cells were trypsinised with 0.5% Trypsin-
686 EDTA (Gibco) then filtered sequentially through 100µm, 70µm and 40µm filters to obtain single cell
687 suspensions and seeded at $1.0x10^5$ cells/well on a TC-treated plastic 24-well plate following CDM
688 production and denuding. Following cell attachment and elongation to matrix (6 hours) media was
689 gently removed and replaced with fresh media containing 1, 3, 5µM GV101 or DMSO control. Wells
690 were imaged every 30 minutes for 12 hours on an IncuCyte S3 Live-Cell Analysis Instrument (Sartorius).
691 Single cell migration was then analysed using CellTracker image processing software [96], with 10 cells
692 per well tracked for four wells per condition for three independent repeats (total 40
693 cells/condition/repeat).

694 Collective Cell Migration Assays

695 Collective cell migration was performed as previously reported [33, 62, 73, 74]. PyMT 20065 cells were
696 trypsinised with 0.5% Trypsin-EDTA (Gibco). Cells were seeded onto denuded TIF derived CDMs at
697 $5.0x10^5$ cells/well. Cells were seeded in media containing 1, 3, 5µM GV101 or DMSO control and
698 imaged at 6 and 24 hours post seeding on an IncuCyte S3 Live-Cell Analysis Instrument (Sartorius). Cell
699 attachment and elongation were assessed via the circularity function in ImageJ at 6 hours post
700 seeding. Growth of cells on CDM and collective cell migration was assessed 24 hours post cell seeding
701 using the ImageJ plugin FibrilTool [75]. Briefly, masks of cells were made from images and images were
702 separated into quadrants before quantification of anisotropy (used as a surrogate readout for
703 collective cell migration) using Fibriltool [75]. Cell growth was quantified using the % of area covered
704 by cell masks in ImageJ. In total, nine regions of interest (ROI) were analysed per well with four wells
705 per condition over three independent repeats.

706 ## Organotypic Invasion Assays

707 Organotypic invasion assays were performed using a modified version of previously published work
708 [33, 57, 59, 62]. Matrices containing $1.67x10^5$ TIFs were treated with 5µM GV101 or DMSO control
709 during contraction, with media and drug changed on days 3, 6 and 9. Following 12 days of contraction
710 fibroblasts were killed with 400ug/mL Hygromycin B (Invitrogen) in growth media for 3 days. Matrices
711 were then transported into individual wells of a TC-treated plastic 24-well plate. MDA-MB-231 cells
712 ($1x10^5$ cells/matrix) were seeded on top of TIF contracted matrices in appropriate growth media. Cells
713 were allowed to grow on top of matrices for 3 days, during which a confluent monolayer was
714 established. Matrices were then transferred onto metal grids which were placed in a 6cm TC treated
715 plastic dish. Growth media containing 5µM GV101 or DMSO control was added to dishes to the level
716 of the metal grid to create an air-liquid interface generating a chemotactic gradient, allowing cancer
717 cells to invade into the collagen matrix. Media was changed every two days for a period of 14 days.
718 Following 14 days of invasion matrices were fixed in 10% formalin for further histopathology
719 processing and H&E staining. Analysis was performed using Qupath [94], with three matrices analysed
720 per condition for three independent repeats. Whole matrices were analysed with sections of matrices
721 with a confluent monolayer of cells on top of the matrices was deemed appropriate for analysis.

722 ## Tissue processing, embedding and microtomy

723 All histopathology was performed in-house at the Histopathology and Biospecimen Facility at the
724 Garvan Institute of Medical Research. Organotypic matrices were fixed in 10% neutral buffered
725 formalin for 24 hours then transferred into 70% Ethanol ready for tissue processing using the Leica
726 Peloris II (Leica Biosystems). During processing samples moved through a graded series of Ethanol
727 concentrations, followed by xylene, then paraffin at 60°C. Samples were then embedded using the
728 TissueTek Embedding Station (Sakura Finetek).

729 Paraffin embedded blocks were sectioned at a thickness of 4µm using a Leica Microtome RM2235
730 (Leica Biosystems). Sections were placed onto Superfrost™ plus slides (Thermo Fisher Scientific) and
731 allowed to incubate for 2 hours in a 60°C oven, for maximum adhesion.
732

733 ## Immunohistochemistry

734 All IHC staining was performed on a Leica Bond RX platform (Leica Biosystems). Slides were dewaxed
735 (Bond Dewax Solution Ref: AR9222), followed by Heat-Induced Epitope Retrieval (HIER) using pH9
736 Epitope Retrieval solution 2 (AR9640, Leica Biosystems) for 20-30 minutes at 93°C for organotypic
737 matrices or 100°C for tissue. Slides were incubated with primary antibody for 60 minutes, followed a
738 secondary antibody (polymer), then visualised with DAB (Bond Polymer Refine Detection Kit DS9800).

739 All IHC slides were counterstained with Haematoxylin (Australian Biostain Haematoxylin Harris non-
740 toxic, acidified) and coverslipped.

741

742 Picrosirius Red Staining

743 Picrosirius red staining was performed on organotypic contraction collagen matrices and tissue as
744 achieved previously [33, 57, 62, 63]. Slides were dewaxed and counterstained with Haematoxylin
745 (Australian Biostain Haematoxylin Harris non-toxic, acidified) for 4 seconds on a Leica ST5010
746 Autostainer XL (Leica Biosystems). Slides were then incubated in 0.02% phosphomolybdic acid for 2
747 minutes and briefly washed in water before a 2 hour incubation in 0.1% Picrosirius Red solution
748 (Australian Biostain solution). This was followed by washes in acidified water prior to dehydration and
749 clearing on a Leica ST5010 Autostainer XL (Leica Biosystems) and coverslipping. For CDMs, the CDMs
750 were stained in wells using the same staining reagents mentioned above.

751

752 Imaging and Analysis

753 Picrosirius Red and Polarised Light Microscopy

754 Picrosirius red stained matrices were prepared as previously described and slides were scanned on
755 the Olympus VS200 slide scanner (Olympus Life Science) at 20x magnification using both brightfield
756 and polarised light imaging modalities. Picrosirius red stained CDMs were imaged on a Leica DM 4000
757 microscope at 20x magnification. Picrosirius red staining was quantified from brightfield images on
758 ImageJ. Five ROIs per matrix were analysed with three matrices per repeat for three independent
759 repeats. Collagen birefringence was quantified using the ImageJ Picrosirius Red Birefringence Analyser
760 macro (https://github.com/TCox-Lab) [63].

761 Second Harmonic Generation Imaging

762 Second harmonic generation (SHG) imaging was performed on formalin fixed CDMs and organotypic
763 matrices. Images were acquired on an inverted Leica DMI 6000 SP8 multiphoton microscope (Leica
764 Biosystems) with a Ti-Sapphire femtosecond laser (Coherent Scientific) excitation source tuned to a
765 wavelength of 880nm. SHG signal was recorded with RLD HyD filters 440/20nm. An image area of
766 512x512 pixels was acquired, using a bidirectional scan with a speed of 400Hz and line averaging of 4.
767 Peak SHG intensity was quantified using an in-house quantification tool previously used [33, 62, 63].
768 Overall, three ROIs per matrix/well were imaged with three matrices per condition for three
769 independent repeats.

770 ## Western Blotting

771 Cells were seeded at a density of $7.5x10^5$ cells for PyMT cancer cells and CAFs, and $9x10^5$ for MDA-MB-
772 231 cells and human CAFs in 10cm TC treated plastic dishes. Following 24 hours of growth cells were
773 treated with 5µM GV101 or DMSO control for one hour for PyMT cancer and MDA-MB-231 cells, 6
774 hours for PyMT CAF and 24 hours for human CAF cells before lysate extraction. Dishes were placed on
775 ice and washed twice with ice-cold PBS. Following removal of final PBS wash ice-cold RIPA buffer
776 (50nM HEPES, 1% Triton X-100, 0.5% Sodium deoxycholate, 0.1% SDS, 0.5mM EDTA, 50mM NaF,
777 10mM Sodium orthovanadate, 1x protease inhibitor cocktail [Complete™ mini, EDTA free, Roche]) was
778 added to cells and incubated on ice for 10 minutes. Lysates were removed from plates with a cell
779 scraper and centrifuged at 13,000 RPM at 4°C for 10 minutes. Supernatant was transferred into fresh
780 Eppendorf tubes on ice and either frozen and stored at -20°C or protein quantification performed.
781 Protein concentration was performed via a Bradford assay (Bio-Red Protein Assay Dye Reagent
782 Concentrate). Lysates were prepared at a final concentration of 2µg/µL in sample buffer (NuPage™
783 LDS sample buffer x4) containing 50mM 1,4-Dithiothreitol (DTT, Invitrogen) which were subsequently
784 denatured by heating at 70°C for 10 minutes. Samples were stored at -20°C and thawed at room
785 temperature for western blotting.

786 Protein lysates (20µg) were separated via gel electrophoresis on a 4-12% Bis-Tris gel (NuPage™,
787 Thermo Fisher Scientific). Following separation proteins were transferred onto a PVDF membrane
788 (Immobilon-P, Millipore) in ice-cold transfer buffer (1.05% glycine, 0.225% Tris, 10% methanol in H_2O)
789 for one hour. Membranes were then blocked in 5% bovine serum albumin (BSA) for one hour at room
790 temperature on a shaking platform. Membranes were then incubated in Phospho-Cofilin primary
791 antibody in Tris-buffered saline (0.1% Tween):1% BSA overnight at 4°C on a shaking platform.
792 Following incubation primary antibody was removed and membranes were washed 5x for 5 minutes
793 each in TBST to remove any unbound antibody. Washed membranes were then incubated in
794 horseradish peroxidase (HRP)-linked secondary antibody for 2 hours at room temperature on a
795 shaking platform before removal and again washed 5x for 5 minutes each in TBST to remove any
796 unbound antibody. DAB signal was detected using ECL Plus reagent for GAPDH or Ultra-Enhanced
797 Chemiluminescence for all other antibodies (Western Lightening ECL, PerkinElmer) on a Fusion FX
798 (Viber) machine. Following detection membranes were incubated for 5 minutes in Restore™ PLUS
799 Western Blot Stripping Buffer (Thermo Fisher Scientific) to remove bound antibodies. Membranes
800 were then incubated in TBST containing 1% skim milk for one hour and then washed in TBST. This
801 blotting procedure was then repeated for Cofilin and then GAPDH antibodies. Densitometry analysis
802 performed on ImageJ and normalised to GAPDH loading control.

803 ## Analysis of TCGA and METABRIC datasets

804 TCGA mRNA expression (RNA seq V2 RSEM) and patient clinical data was downloaded for 1040
805 patients with breast ductal, lobular, mixed or breast carcinoma. TNBC patients were defined as ER, PR
806 and HER2 negative on IHC. For survival analysis, patients diagnosed as stage I-III were included (999
807 patients). Patients were separated based on ROCK2 expression levels split in 50% high and 50% low
808 ROCK2 expression. METABRIC ROCK2 mRNA expression (Illumina HT-12 v3 microarray) and patient
809 clinical data was downloaded for 1936 patients with invasive breast ductal, lobular or mixed
810 carcinoma. For survival analysis only patients who were either alive at last follow-up or died of disease
811 were included (n=1449 patients). Patients were stratified into tertiles based on ROCK2 expression.

812 ## Tumour microarray analysis

813 Two tumour microarray (TMA) cohorts, Garvan/Royal Prince Alfred Hospital (RPAH) Breast
814 Progression Series and RPAH/Concord Repatriation General Hospital (CRGH) TNBC cohort, were
815 obtained for ROCK2 immuno-histochemistry (IHC) staining and analysis. Both TMA cohorts were
816 graded and reviewed by a trained breast pathologist at time of construction. Analysis was performed
817 using Qupath image analysis software. A total of 130 patients were used in the analysis of the
818 Garvan/RPAH Breast Progression series and 123 patients in the RPAH/CRGH TNBC cohort. For survival
819 analysis patients were stratified based on high (50%) or low (50%) ROCK2 stain coverage and/or
820 intensity.

Figures and Figure legends

Figure 1

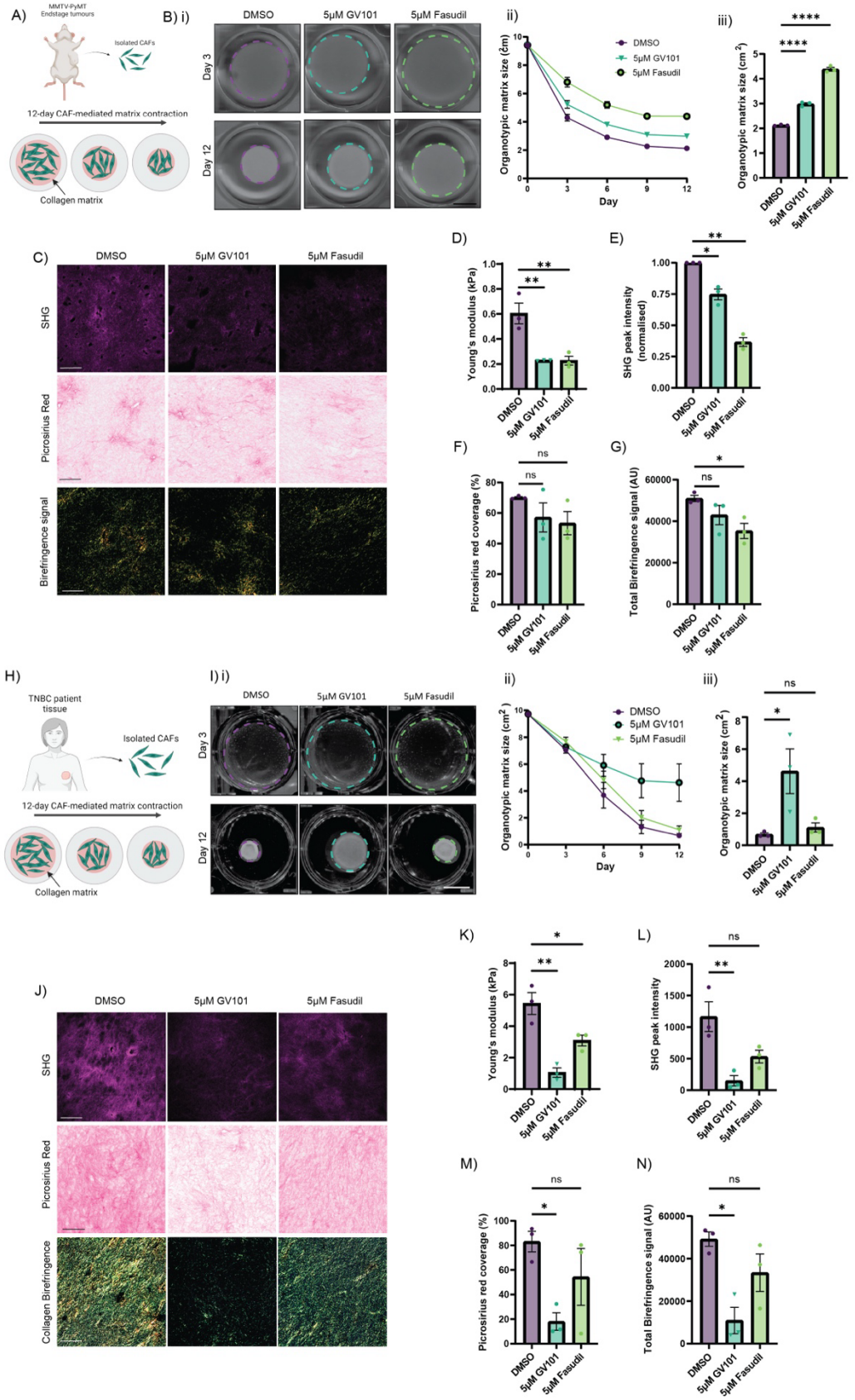

824 Figure 1: ROCK2 inhibition with GV101 reduces CAF-mediated remodelling of pre-
825 existing collagen in murine and human models of TNBC, also see Figures S1 and S2
826 **(A)** Schematic of collagen contraction assays utilising CAFs isolated from end-stage MMTV-PyMT
827 tumours. **(B)** Representative images of PyMT CAF matrices treated with DMSO, GV101 or Fasudil at
828 days 3 and 12 of contraction (i) and quantification of PyMT CAF organotypic matrix size over a 12-day
829 contraction period (ii) and on day 12 (iii). **(C)** Representative SHG images of PyMT CAF matrices to
830 assess collagen I (top panel, magenta), picrosirius red staining to assess fibrillar collagen (middle panel)
831 and polarised light birefringence imaging to assess collagen bundling and density (bottom panel). **(D)**
832 Quantification of unconfined compression analysis to assess Young's modulus. **(E-G)** Quantification of
833 PyMT CAF matrices; SHG peak signal intensity **(E)**, picrosirius red staining coverage **(F)** and total
834 birefringence signal **(G)**. **(H)** Schematic of collagen contraction assays utilising CAFs isolated from
835 human TNBC patients. **(I)** Representative images of human CAF matrices treated with DMSO, GV101
836 or Fasudil at days 3 and 12 of contraction (i) and quantification of CAF organotypic matrix size over a
837 12-day contraction period (ii) and on day 12 (iii). **(J)** Representative SHG images of human CAF matrices
838 to assess collagen I (top panel, magenta), picrosirius red staining to assess fibrillar collagen (middle
839 panel) and polarised light birefringence imaging to assess collagen bundling and density (bottom
840 panel). **(K)** Quantification of unconfined compression analysis to assess matrix Young's modulus. **(L-N)**
841 Quantification of human CAF matrices; SHG peak signal intensity **(L)**, picrosirius red staining coverage
842 **(M)** and total birefringence signal **(N)**. Data represents mean ± SEM of three individual repeats. p-
843 values were determined using One-sample t and Wilcoxon test for normalised data and for remaining
844 data a One-way ANOVA with multiple comparisons was used. ns = not significant ($p \geq 0.05$), * = $p<0.05$,
845 ** = $p<0.01$, *** = $p<0.001$, **** = $p<0.0001$. Scale bar = 1cm (B and I), 100µm (C and J).

846

847 Figure 2

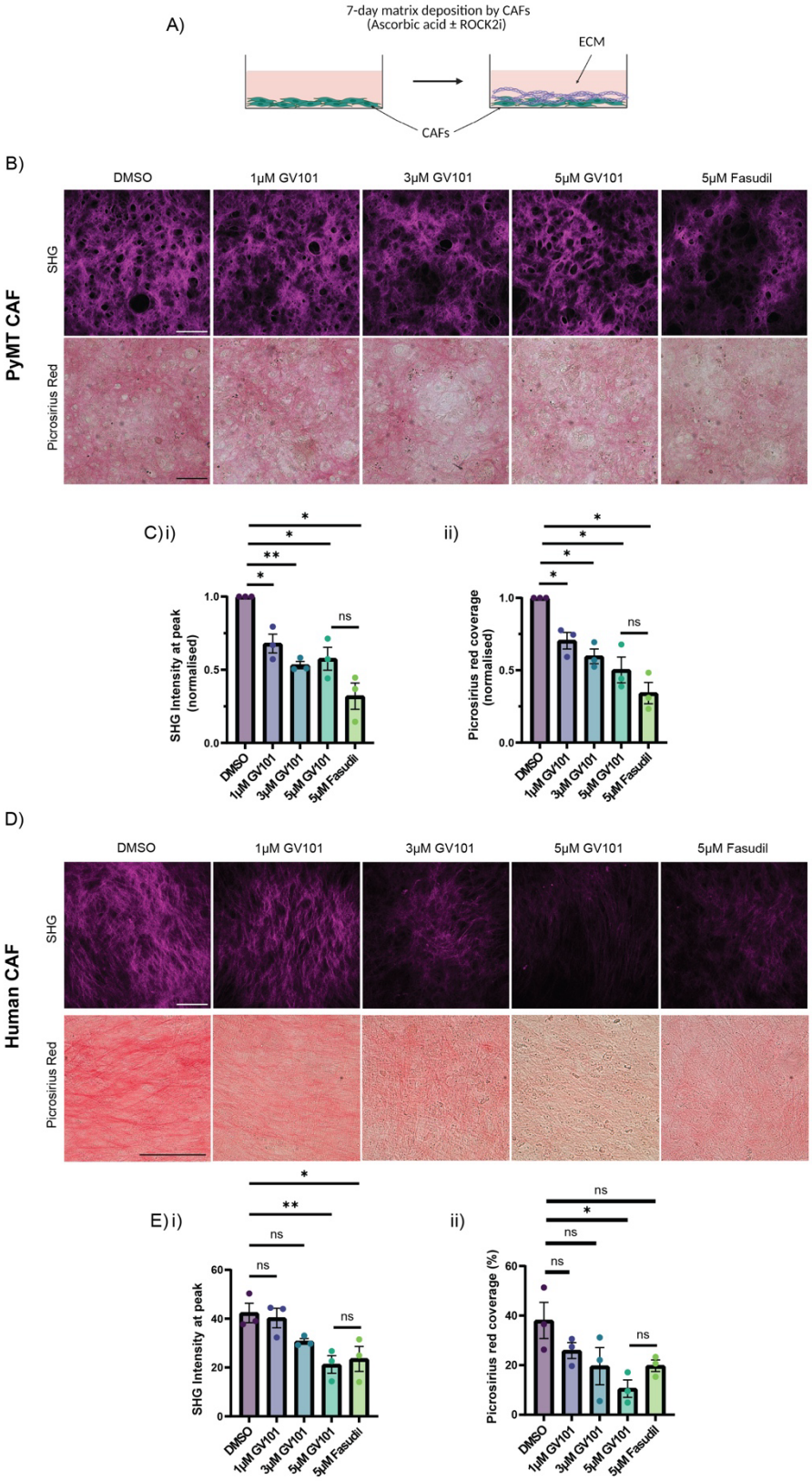

848

849 ## Figure 2: GV101 inhibits CAF-mediated remodelling of *de novo* synthesised collagen in
850 cell-derived matrix assays

851 **(A)** Schematic of cell-derived matrix (CDM) production assays where both PyMT and human CAFs are
852 treated with ascorbic acid to stimulate matrix production in the presence of DMSO, GV101 or Fasudil.
853 **(B)** Representative images of PyMT CAF derived CDMs showing SHG imaging (top panel, magenta) and
854 picrosirius red stained matrices (bottom panel). **(C)** Quantification of peak SHG signal (i) and picrosirius
855 red staining coverage for PyMT CAF generated CDMs (ii). **(D)** Representative images of human CAF
856 derived CDMs showing SHG imaging (top panel, magenta) and picrosirius red stained matrices (bottom
857 panel). **(E)** Quantification of peak SHG signal (i) and picrosirius red coverage (ii) for human CAF
858 generated CDMs. Data represents mean ± SEM of three individual repeats. p-values were determined
859 using One-sample t and Wilcoxon test for normalised data and for remaining data a One-way ANOVA
860 with multiple comparisons was used. ns = not significant ($p \geq 0.05$), * = $p<0.05$, ** = $p<0.01$. Scale bar
861 = 100µm.

862

Figure 3

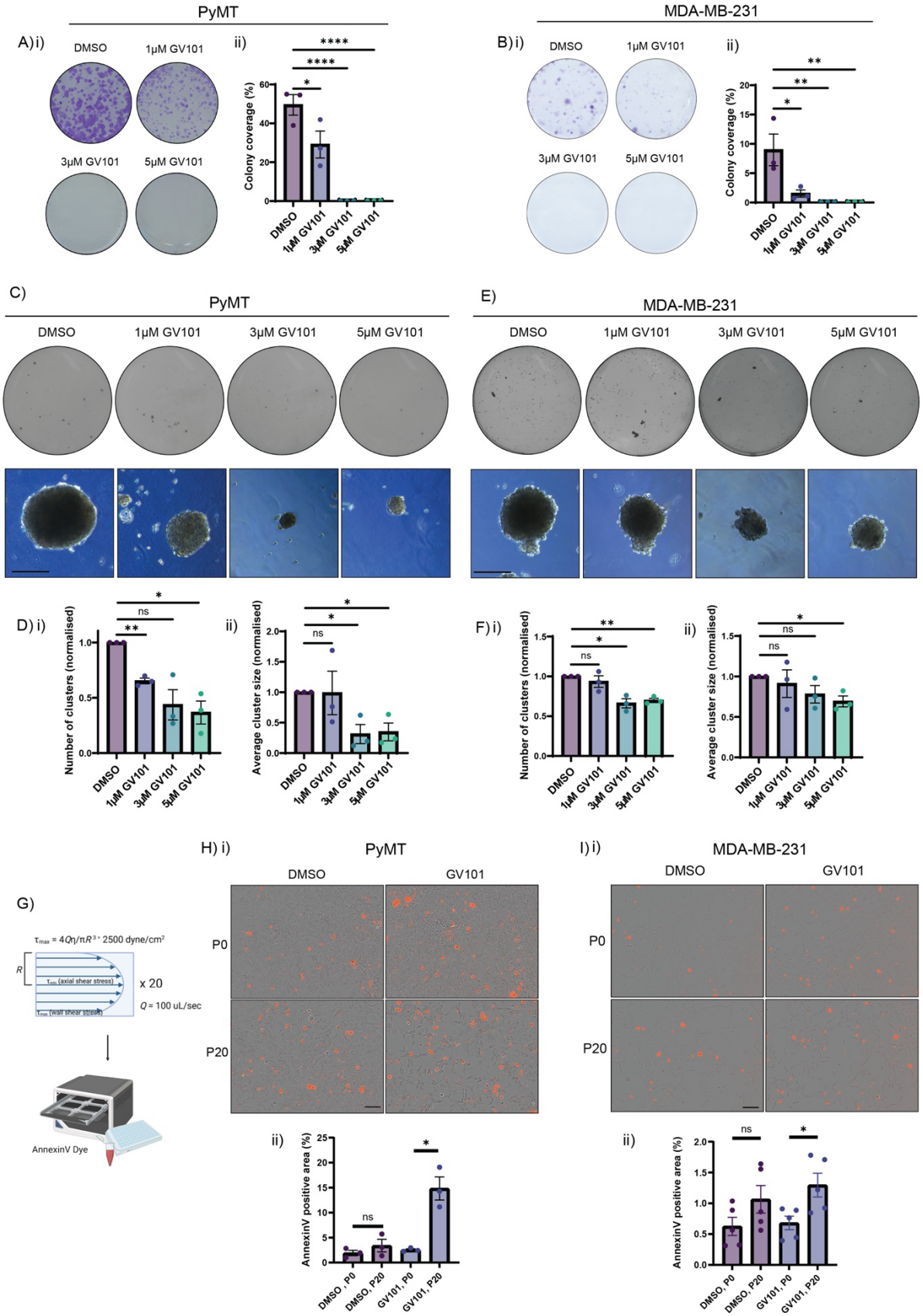
PyMT
A) i)
DMSO
1μM GV101
3μM GV101
5μM GV101
ii)
Colony coverage (%)
MDA-MB-231
B) i)
C)
D) i)
Number of clusters (normalised)
ii)
Average cluster size (normalised)
E)
F) i)
G)
$\tau_{max} = 4Q\eta/\pi R^3 = 2500$ dyne/cm²
x 20
Q = 100 uL/sec
AnnexinV Dye
H) i)
GV101
P0
P20
I) i)
AnnexinV positive area (%)
DMSO, P0
DMSO, P20
GV101, P0
GV101, P20

865 Figure 3: ROCK2 inhibition with GV101 reduces epithelial cell outgrowth in 2D and 3D
866 while also sensitising cells to fluid flow-induced shear stress, also see Figure S3

867 **(A)** Representative images of PyMT cancer cell 2D colony formation assay stained with crystal violet
868 to visualise colonies following 4 days of treatment (i) and quantification of colonies (ii). **(B)**
869 Representative images of MDA-MB-231 2D colony formation assays stained with crystal violet to
870 visualise colonies following 4 days of treatment (i) and quantification of colonies (ii). **(C)**
871 Representative images of whole wells stained with quick-dip II to visualise PyMT cancer cell AIG
872 clusters (top panel) and representative images of individual AIG clusters (bottom panel). **(D)**
873 Quantification of PyMT cancer cell AIG cluster number (i) and average cluster size (ii). **(E)**
874 Representative images of whole wells stained with quick-dip II to visualise MDA-MB-231 AIG clusters
875 (top panel) and representative images of individual AIG clusters (bottom panel). **(F)** Quantification of
876 MDA-MB-231 cancer cell AIG cluster number (i) and average cluster size (ii). **(G**) Schematic of shear
877 stress assay to assess GV101 treatment following fluid flow-induced shear stress using AnnexinV
878 incucyte imaging. **(H)** Representative images of PyMT cancer cells after fluid flow-induced shear stress
879 (P0 = no shear stress, P20 = 20 cycles of shear stress) and subsequent treatment with DMSO or GV101
880 and AnnexinV dye (red) to visualise cell apoptosis (i) and quantification of PyMT cancer cell apoptosis
881 at 24 hours after fluid flow-induced shear stress (ii). **(I)** Representative images of MDA-MB-231 cancer
882 cells after fluid flow-induced shear stress (P0 = no shear stress, P20 = 20 cycles of shear stress) and
883 subsequent treatment with DMSO or GV101 and AnnexinV dye (red) to visualise cell apoptosis (i) and
884 quantification of MDA-MB-231 cancer cell apoptosis at 24 hours after fluid flow-induced shear stress
885 (ii). Data represents mean ± SEM of three individual repeats. p-values were determined using One-
886 sample t test for normalised data and Unpaired t-test for remaining data was used. For shear stress
887 analysis an unpaired t test was used. ns = not significant ($p \geq 0.05$), * = $p<0.05$, ** = $p<0.01$, **** =
888 $p<0.0001$. Scale bar = 150µm.

889

890 ## Figure 4

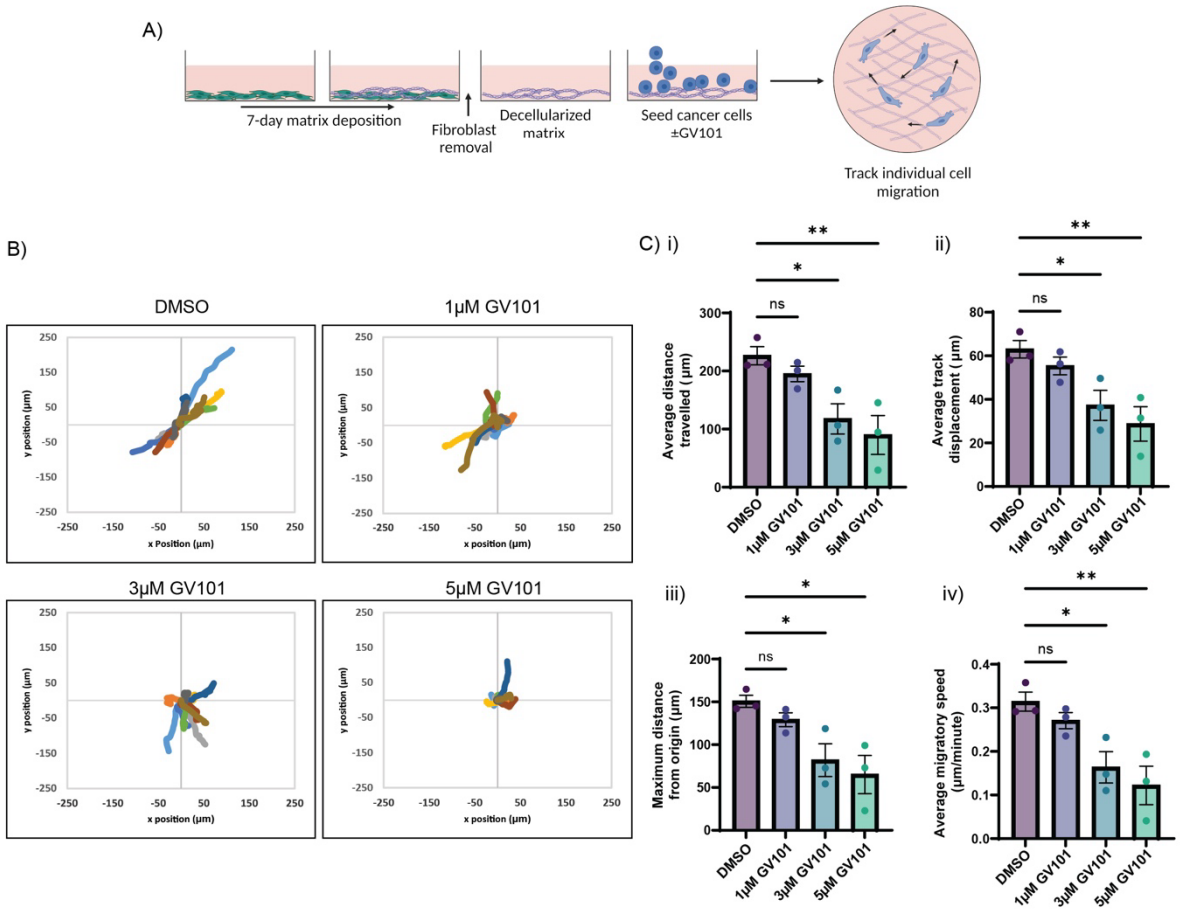

891

892 Figure 4: ROCK2 inhibition with GV101 decreases the single-cell migratory capacity of
893 epithelial cells on cell-derived matrices

894 **(A)** Schematic of single-cell migration assay where MDA-MB-231 cells were seeded on cell-derived
895 (CDMs), treated with GV101 and individual migratory patterns tracked over a 12-hour period. **(B)**
896 Representative polar plots showing cell migratory tracks of individual cells (depicted as individually
897 coloured tracks) from a starting point (origin) over 12 hours of migration. **(C)** Quantification of single
898 cell migration showing average distance travelled (i), average track displacement (ii), maximum
899 distance from origin (iii) and average migratory speed (iv). Data represents mean ± SEM of three
900 individual repeats, with 40 cells/condition/repeat analysed. p-values were determined using a One-
901 way ANOVA with multiple comparisons, ns = not significant ($p \geq 0.05$), * = $p<0.05$, ** = $p<0.01$.

902

Figure 5

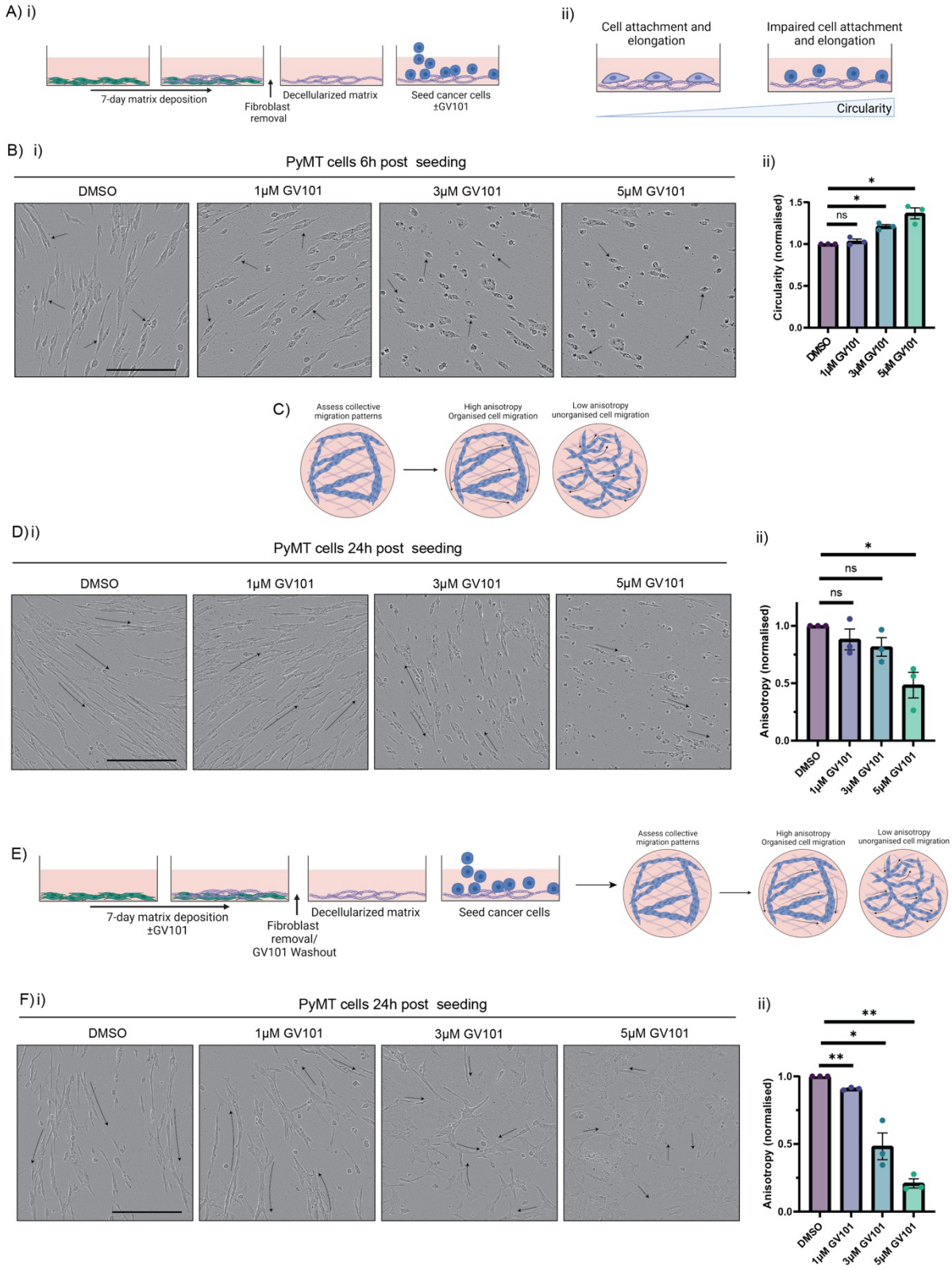
A) i)
7-day matrix deposition
Fibroblast removal
Decellularized matrix
Seed cancer cells ±GV101
ii)
Cell attachment and elongation
Impaired cell attachment and elongation
Circularity
B) i)
PyMT cells 6h post seeding
DMSO
1μM GV101
3μM GV101
5μM GV101
ii)
Circularity (normalised)
ns
*
C)
Assess collective migration patterns
High anisotropy Organised cell migration
Low anisotropy unorganised cell migration
D) i)
PyMT cells 24h post seeding
DMSO
1μM GV101
3μM GV101
5μM GV101
ii)
Anisotropy (normalised)
ns
*
E)
7-day matrix deposition ±GV101
Fibroblast removal/ GV101 Washout
Decellularized matrix
Seed cancer cells
Assess collective migration patterns
High anisotropy Organised cell migration
Low anisotropy unorganised cell migration
F) i)
PyMT cells 24h post seeding
DMSO
1μM GV101
3μM GV101
5μM GV101
ii)
Anisotropy (normalised)
**
*

905 ## Figure 5: GV101 treatment of stromal ROCK2 reduces collective cell migration

906 **(A)** Schematic of cell-derived matrix (CDM) generation assay (i) and schematic of cell attachment and
907 elongation on CDM to assess circularity (ii). **(B)** Representative images of PyMT cancer cell landing on
908 a CDM following 6 hours of treatment with DMSO or GV101 (i) and quantification of PyMT cell
909 circularity upon 6 hours of treatment (ii). **(C)** Schematic of collective cell migration showing organised
910 (high anisotropy) and unorganised (low anisotropy) cell migration. **(D)** Representative images of PyMT
911 cancer cell collective migration on a CDM following 24 hours of treatment with DMSO or GV101 (i)
912 and quantification of PyMT collective cell migration *via* anisotropy (ii). **(E)** Schematic of CDM
913 generation and PyMT cancer cell streaming assay upon GV101 treatment of fibroblasts during matrix
914 deposition and assessment of cell streaming *via* anisotropy. **(F)** Representative images of PyMT cancer
915 cells 24 hours post seeding on a GV101 pre-treated matrix (i) and quantification of collective cell
916 migration *via* anisotropy (ii). Data represents mean ± SEM of three individual repeats. Data represents
917 mean ± SEM of three individual repeats. p-values were determined using One-sample t test , ns = not
918 significant ($p \geq 0.05$), * = $p<0.05$, ** = $p<0.01$. Scale bar = 200µm.

919

920 Figure 6

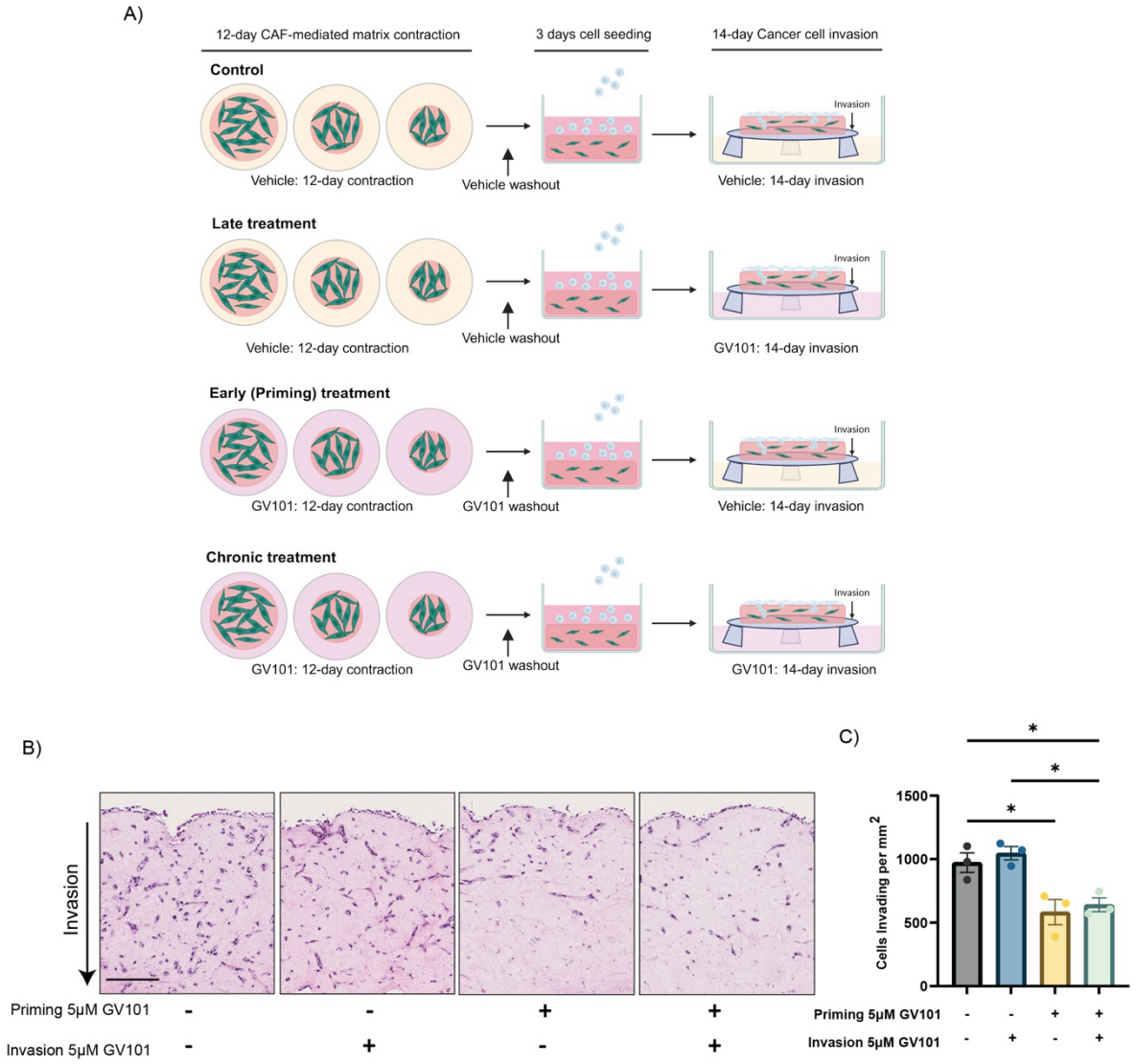

921

922 Figure 6: Disruption of stromal matrix remodelling impairs cell invasion into 3D
923 organotypic collagen matrices

924 **(A)** Schematic of organotypic invasion assay showing fibroblast-mediated collagen contraction, cancer
925 cell seeding and subsequent invasion into contracted matrices towards a chemotactic gradient. **(B)**
926 Representative images of H&E-stained cross-sections of MDA-MB-231 cancer cell organotypic
927 invasion assays with cancer cell invasion into the matrix assessed upon early stromal priming, late
928 invasion treatment or continuous (chronic) treatment with GV101. **(C)** Quantification of number of
929 MDA-MB-231 cancer cells invading into the matrix per mm^2. Data represents mean ± SEM of three
930 individual repeats. p-values were determined using a One-way ANOVA with multiple comparisons. *
931 = $p<0.05$. Scale bar = 100μm.

932

933 Figure 7

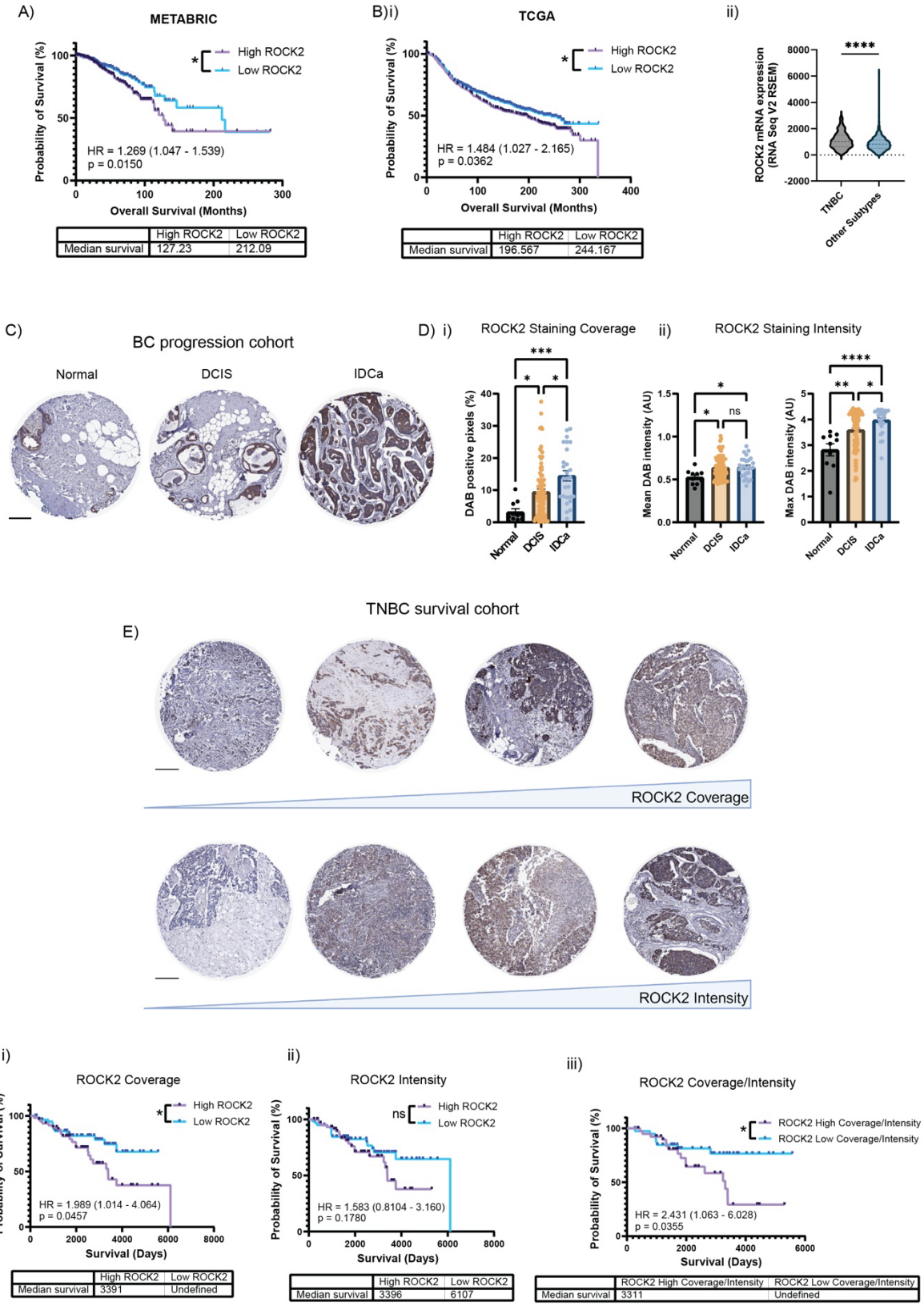

934

935 Figure 7: High ROCK2 expression correlates with disease progression and poorer
936 survival in human breast cancer cohorts

937 **(A)** Survival analysis of breast cancer (BC) patients from the METABRIC BC patient cohort stratifying
938 patients based on ROCK2 mRNA expression. **(B)** Analysis of the TCGA BC patient cohort assessing
939 ROCK2 mRNA expression on patient survival (i) and comparing ROCK2 mRNA expression levels in
940 triple-negative breast cancer (TNBC) patients to all other BC subtypes (ii). **(C)** Representative images
941 of TMA cores from the Garvan/RPA Breast Progression Series stained with immunohistochemistry for
942 ROCK2. **(D)** Quantification of ROCK2 staining coverage (i) and staining intensity (ii) in the Garvan/RPA
943 Breast Progression Series TMA cohort. **(E)** Representative images of TMA cores stained with
944 immunohistochemistry for ROCK2 from the RPA/CRGH TNBC TMA cohort showing increasing ROCK2
945 staining coverage and intensity. **(F)** Survival analysis assessing ROCK2 staining coverage (i), intensity
946 (ii) and combined coverage and intensity (iii). For survival curves p-values were determined using Log-
947 rank (Mantel-Cox) test and hazard rations (HR) with 95% confidence interval by a univariate Cox
948 Proportional Hazards Model. For subtype comparison Unpaired t-test was used and for disease
949 progression an Ordinary one-way ANOVA with multiple comparisons was used. * = $p<0.05$, ** =
950 $p<0.01$, *** = $p<0.001$, **** = $p<0.0001$. Scale bar = 200µm.

951

952 # Supplementary Figure legends

953 ## Supplementary Figure S1: GV101 reduces ROCK2 signalling and collagen remodelling by
954 PyMT and human CAFs, related to Figure 1

955 **(A)** Representative western blot images showing ROCK2 protein expression in PyMT and Human TNBC
956 CAFs. **(B)** Representative western blot images showing total and phosphorylated Cofilin (pCofilin) of
957 PyMT CAFs following treatment with DMSO or GV101 (i) and quantification of pCofilin levels relative
958 to total cofilin (ii). (**C)** Representative western blot images showing total and pCofilin of human TNBC
959 CAFs following treatment with DMSO or GV101 (i) and quantification of pCofilin levels relative to total
960 cofilin (ii). **(D-G)** Representative images of individual birefringence signal channels for picrosirius red
961 stained PyMT CAF matrices **(D)** and quantification of birefringence signal showing contribution of
962 green **(E)**, yellow **(F)** and red-orange **(G)** birefringence signal. **(H-K)** Representative images of individual
963 birefringence signal channels for picrosirius red stained Human TNBC CAF matrices **(H)** and
964 quantification of birefringence signal showing contribution of green **(I)**, yellow **(J)** and red-orange **(K)**
965 birefringence signal to the total birefringence signal. Data represents mean ± SEM of three individual
966 repeats. p-values were determined using a One-way ANOVA with multiple comparisons. ns = not
967 significant ($p \geq 0.05$), * = $p<0.05$. Scale bar = 100µm.

968

969 ## Supplementary Figure S2: GV101 reduces ROCK2 signalling and cell viability in PyMT
970 and MDA-MB-231 TNBC cell lines, related to Figure 2

971 **(A)** Representative western blot images showing ROCK2 protein expression in PyMT 20065 and MDA-
972 MB-231 cancer cells. **(B)** Representative western blot images showing total and phosphorylated Cofilin
973 (pCofilin) of PyMT cancer cells following treatment with DMSO or GV101 (i) and quantification of
974 pCofilin levels relative to total cofilin (ii). **(C)** Representative images of western blot showing total and
975 pCofilin of MDA-MB-231 cells following treatment with DMSO or GV101 (i) and quantification of
976 pCofilin levels relative to total cofilin (ii). **(D)** Quantification of cell viability of PyMT cancer cells
977 following treatment with DMSO, GV101 or Fasudil. **(E)** Quantification of cell viability of MDA-MB-231
978 cells following treatment with DMSO, GV101 or Fasudil. Data represents mean ± SEM of three
979 individual repeats. p-values were determined using One-sample t test. ns = not significant ($p \geq 0.05$), *
980 = $p<0.05$, ** = $p<0.01$.

981 Supplementary Figure S3: Analysis workflow for cell apoptosis quantification following
982 exposure to fluid flow-induced shear stress, related to Figure 2 and STAR Methods

983 **(A)** Cellpose was used to segment cells in phase images and generate a cell coverage mask. **(B)**
984 Matched AnnexinV masks were generated and superimposed on the corresponding cell coverage
985 masks to determine AnnexinV signal per individual cell.

986 # Supplementary Movie legends

987 ## Supplementary Movie 1: GV101 reduces remodelling of pre-existing collagen by PyMT
988 CAFs, related to Figure 1

989 Z-stacks of SHG signal through PyMT CAF-contracted collagen matrices (Day 12 of contraction)
990 following treatment with DMSO, GV101 or Fasudil. Scale bar = 150µm.

991

992 ## Supplementary Movie S2: GV101 reduces remodelling of pre-existing collagen by
993 human TNBC CAFs, related to Figure 1

994 Z-stacks of SHG signal through human CAF-contracted collagen matrices (Day 12 of contraction)
995 following treatment with DMSO, GV101 or Fasudil. Scale bar = 150µm.

996

997 ## Supplementary Movie S3: GV101 reduces remodelling of *de novo* synthesised collagen
998 by PyMT CAFs, related to Figure 2

999 Z-stacks of SHG signal through PyMT CAF-generated CDMs (Day 7 of CDM generation) following
1000 treatment with DMSO, GV101 or Fasudil. Scale bar = 150µm.

1001

1002 ## Supplementary Movie S4: GV101 reduces remodelling of *de novo* synthesised collagen
1003 by PyMT CAFs, related to Figure 2

1004 Z-projections of SHG signal through PyMT CAF-generated CDMs (Day 7 of CDM generation) following
1005 treatment with DMSO, GV101 or Fasudil. Scale bar = 30µm.

1006

1007 ## Supplementary Movie S5: GV101 reduces remodelling of *de novo* synthesised collagen
1008 by human TNBC CAFs, related to Figure 2

1009 Z-stacks of SHG signal through human CAF-generated CDMs (Day 7 of CDM generation) following
1010 treatment with DMSO, GV101 or Fasudil. Scale bar = 150µm.

1011

1012 ## Supplementary Movie S6: GV101 reduces remodelling of *de novo* synthesised collagen
1013 by human TNBC CAFs, related to Figure 2

1014 Z-projections of SHG signal through human CAF-generated CDMs (Day 7 of CDM generation) following
1015 treatment with DMSO, GV101 or Fasudil. Scale bar = 30µm.

1016

1017 ## Supplementary Movie S7: GV101 reduces single-cell migration of MDA-MB-231 cells on
1018 CDMs, related to Figure 4

1019 Time-lapse movies of MDA-MB-231 single-cell migration on CDMs over 12 hours in the presence of
1020 DMSO or GV101. Scale bar = 400µm.

1021

1022 ## Supplementary Movie S8: GV101-mediated inhibition of epithelial ROCK2 reduces
1023 PyMT cell attachment and spreading on CDMs without significantly affecting
1024 subsequent collective cell migration, related to Figure 5

1025 Time-lapse movies of PyMT cell attachment and spreading on CDMs and subsequent collective cell
1026 migration over 24 hours in the presence of DMSO or GV101 (inhibition of epithelial ROCK2). Scale bar
1027 = 400µm.

1028

1029 ## Supplementary Movie S9: GV101-mediated inhibition of stromal ROCK2 during CDM
1030 generation is sufficient to reduce subsequent PyMT collective cell migration, related to
1031 Figure 5

1032 Time-lapse movies of PyMT collective cell migration over 24 hours on CDMs that were generated in
1033 the presence of DMSO or GV101 (inhibition of stromal ROCK2). Scale bar = 400µm.

1034 # References

1035 1. Julian, L. and M.F. Olson, *Rho-associated coiled-coil containing kinases (ROCK): structure,*
1036 *regulation, and functions.* Small GTPases, 2014. **5**: p. e29846.
1037 2. Shi, J., et al., *Distinct roles for ROCK1 and ROCK2 in the regulation of cell detachment.* Cell
1038 Death Dis, 2013. **4**(2): p. e483.
1039 3. Amano, M., et al., *Phosphorylation and activation of myosin by Rho-associated kinase (Rho-*
1040 *kinase).* J Biol Chem, 1996. **271**(34): p. 20246-9.
1041 4. Kimura, K., et al., *Regulation of myosin phosphatase by Rho and Rho-associated kinase (Rho-*
1042 *kinase).* Science, 1996. **273**(5272): p. 245-8.
1043 5. Barcelo, J., R. Samain, and V. Sanz-Moreno, *Preclinical to clinical utility of ROCK inhibitors in*
1044 *cancer.* Trends Cancer, 2023. **9**(3): p. 250-263.
1045 6. Provenzano, P.P. and P.J. Keely, *Mechanical signaling through the cytoskeleton regulates cell*
1046 *proliferation by coordinated focal adhesion and Rho GTPase signaling.* J Cell Sci, 2011. **124**(Pt
1047 8): p. 1195-205.
1048 7. Croft, D.R. and M.F. Olson, *The Rho GTPase effector ROCK regulates cyclin A, cyclin D1, and*
1049 *p27Kip1 levels by distinct mechanisms.* Mol Cell Biol, 2006. **26**(12): p. 4612-27.
1050 8. Street, C.A. and B.A. Bryan, *Rho kinase proteins--pleiotropic modulators of cell survival and*
1051 *apoptosis.* Anticancer Res, 2011. **31**(11): p. 3645-57.
1052 9. Gao, L., et al., *Post-Passage rock inhibition induces cytoskeletal aberrations and apoptosis in*
1053 *Human embryonic stem cells.* Stem Cell Res, 2019. **41**: p. 101641.
1054 10. Kümper, S., et al., *Rho-associated kinase (ROCK) function is essential for cell cycle progression,*
1055 *senescence and tumorigenesis.* Elife, 2016. **5**: p. e12994.
1056 11. Patel, R.A., et al., *RKI-1447 is a potent inhibitor of the Rho-associated ROCK kinases with anti-*
1057 *invasive and antitumor activities in breast cancer.* Cancer Res, 2012. **72**(19): p. 5025-34.
1058 12. Patel, R.A., et al., *Identification of novel ROCK inhibitors with anti-migratory and anti-invasive*
1059 *activities.* Oncogene, 2014. **33**(5): p. 550-5.
1060 13. Sadok, A. and C.J. Marshall, *Rho GTPases: masters of cell migration.* Small GTPases, 2014. **5**:
1061 p. e29710.
1062 14. Schackmann, R.C., et al., *Cytosolic p120-catenin regulates growth of metastatic lobular*
1063 *carcinoma through Rock1-mediated anoikis resistance.* J Clin Invest, 2011. **121**(8): p. 3176-88.
1064 15. Vargas-Accarino, E., et al., *Spontaneous Cell Detachment and Reattachment in Cancer Cell*
1065 *Lines: An In Vitro Model of Metastasis and Malignancy.* Int J Mol Sci, 2021. **22**(9).
1066 16. Vigil, D., et al., *ROCK1 and ROCK2 are required for non-small cell lung cancer anchorage-*
1067 *independent growth and invasion.* Cancer Res, 2012. **72**(20): p. 5338-47.
1068 17. van de Ven, R.A., et al., *Nuclear p120-catenin regulates the anoikis resistance of mouse lobular*
1069 *breast cancer cells through Kaiso-dependent Wnt11 expression.* Dis Model Mech, 2015. **8**(4):
1070 p. 373-84.
1071 18. Kang, H., et al., *Vascular smooth muscle cell glycocalyx mediates shear stress-induced*
1072 *contractile responses via a Rho kinase (ROCK)-myosin light chain phosphatase (MLCP)*
1073 *pathway.* Sci Rep, 2017. **7**: p. 42092.
1074 19. Lee, H.J., et al., *Fluid shear stress activates YAP1 to promote cancer cell motility.* Nat Commun,
1075 2017. **8**: p. 14122.
1076 20. Samuel, M.S., et al., *Actomyosin-mediated cellular tension drives increased tissue stiffness and*
1077 *β-catenin activation to induce epidermal hyperplasia and tumor growth.* Cancer Cell, 2011.
1078 **19**(6): p. 776-91.
1079 21. Boyle, S.T., et al., *ROCK-mediated selective activation of PERK signalling causes fibroblast*
1080 *reprogramming and tumour progression through a CRELD2-dependent mechanism.* Nat Cell
1081 Biol, 2020. **22**(7): p. 882-895.
1082 22. Porazinski, S., A. Parkin, and M. Pajic, *Rho-ROCK Signaling in Normal Physiology and as a Key*
1083 *Player in Shaping the Tumor Microenvironment.* Adv Exp Med Biol, 2020. **1223**: p. 99-127.

1084 23. Crosas-Molist, E., et al., *Rho GTPase signaling in cancer progression and dissemination.* Physiol
1085 Rev, 2022. **102**(1): p. 455-510.
1086 24. Nakagawa, O., et al., *ROCK-I and ROCK-II, two isoforms of Rho-associated coiled-coil forming*
1087 *protein serine/threonine kinase in mice.* FEBS Lett, 1996. **392**(2): p. 189-93.
1088 25. Amano, M., Y. Fukata, and K. Kaibuchi, *Regulation and functions of Rho-associated kinase.* Exp
1089 Cell Res, 2000. **261**(1): p. 44-51.
1090 26. Montagnoli, T.L., et al., *ROCK Inhibition as Potential Target for Treatment of Pulmonary*
1091 *Hypertension.* Cells, 2021. **10**(7).
1092 27. Koch, J.C., et al., *ROCK inhibition in models of neurodegeneration and its potential for clinical*
1093 *translation.* Pharmacol Ther, 2018. **189**: p. 1-21.
1094 28. Fujimura, M., F. Usuki, and A. Nakamura, *Fasudil, a Rho-Associated Coiled Coil-Forming Protein*
1095 *Kinase Inhibitor, Recovers Methylmercury-Induced Axonal Degeneration by Changing*
1096 *Microglial Phenotype in Rats.* Toxicol Sci, 2019. **168**(1): p. 126-136.
1097 29. He, Y., et al., *Antiinflammatory effect of Rho kinase blockade via inhibition of NF-kappaB*
1098 *activation in rheumatoid arthritis.* Arthritis Rheum, 2008. **58**(11): p. 3366-76.
1099 30. Biswas, P.S., et al., *Phosphorylation of IRF4 by ROCK2 regulates IL-17 and IL-21 production and*
1100 *the development of autoimmunity in mice.* J Clin Invest, 2010. **120**(9): p. 3280-95.
1101 31. Zhou, Y., et al., *Inhibition of mechanosensitive signaling in myofibroblasts ameliorates*
1102 *experimental pulmonary fibrosis.* J Clin Invest, 2013. **123**(3): p. 1096-108.
1103 32. Shimizu, Y., et al., *Contribution of small GTPase Rho and its target protein rock in a murine*
1104 *model of lung fibrosis.* Am J Respir Crit Care Med, 2001. **163**(1): p. 210-7.
1105 33. Vennin, C., et al., *Transient tissue priming via ROCK inhibition uncouples pancreatic cancer*
1106 *progression, sensitivity to chemotherapy, and metastasis.* Sci Transl Med, 2017. **9**(384).
1107 34. Rath, N., et al., *ROCK signaling promotes collagen remodeling to facilitate invasive pancreatic*
1108 *ductal adenocarcinoma tumor cell growth.* EMBO Mol Med, 2017. **9**(2): p. 198-218.
1109 35. Calvo, F., et al., *Mechanotransduction and YAP-dependent matrix remodelling is required for*
1110 *the generation and maintenance of cancer-associated fibroblasts.* Nature Cell Biology, 2013.
1111 **15**(6): p. 637-646.
1112 36. Wu, H., et al., *Targeting ROCK1/2 blocks cell division and induces mitotic catastrophe in*
1113 *hepatocellular carcinoma.* Biochem Pharmacol, 2021. **184**: p. 114353.
1114 37. Dyberg, C., et al., *Rho-associated kinase is a therapeutic target in neuroblastoma.* Proc Natl
1115 Acad Sci U S A, 2017. **114**(32): p. E6603-e6612.
1116 38. de Sousa, G.R., et al., *Should we keep rocking? Portraits from targeting Rho kinases in cancer.*
1117 Pharmacol Res, 2020. **160**: p. 105093.
1118 39. Averill, F., et al., *A phase 2 trial of KD025 to assess efficacy, safety and tolerability in patients*
1119 *with idiopathic pulmonary fibrosis*, in *C97. Diffuse Parenchymal Lung Diseases: Evaluation,*
1120 *Outcomes, and Trials*. 2018, American Thoracic Society. p. A5927-A5927.
1121 40. DeFilipp, Z., et al., *Clinical response to belumosudil in bronchiolitis obliterans syndrome: a*
1122 *combined analysis from 2 prospective trials.* Blood Adv, 2022. **6**(24): p. 6263-6270.
1123 41. Nalkurthi, C., et al., *ROCK2 inhibition attenuates profibrogenic immune cell function to reverse*
1124 *thioacetamide-induced liver fibrosis.* JHEP Rep, 2022. **4**(1): p. 100386.
1125 42. Zanin-Zhorov, A., et al., *Cutting Edge: Selective Oral ROCK2 Inhibitor Reduces Clinical Scores in*
1126 *Patients with Psoriasis Vulgaris and Normalizes Skin Pathology via Concurrent Regulation of*
1127 *IL-17 and IL-10.* J Immunol, 2017. **198**(10): p. 3809-3814.
1128 43. Zanin-Zhorov, A., et al., *Selective oral ROCK2 inhibitor down-regulates IL-21 and IL-17 secretion*
1129 *in human T cells via STAT3-dependent mechanism.* Proc Natl Acad Sci U S A, 2014. **111**(47): p.
1130 16814-9.
1131 44. Devkota, R., et al., *KD025 Is a Casein Kinase 2 Inhibitor That Protects Against Glucolipotoxicity*
1132 *in β-Cells.* Diabetes, 2024. **73**(4): p. 585-591.
1133 45. Jagasia, M., et al., *ROCK2 Inhibition With Belumosudil (KD025) for the Treatment of Chronic*
1134 *Graft-Versus-Host Disease.* J Clin Oncol, 2021. **39**(17): p. 1888-1898.

46. Jing, W., et al., *KD025, an anti-adipocyte differentiation drug, enhances the efficacy of conventional chemotherapeutic drugs in ABCG2-overexpressing leukemia cells.* Oncol Lett, 2020. **20**(6): p. 309.
47. Zanin-Zhorov, A., et al., *Selectivity matters: selective ROCK2 inhibitor ameliorates established liver fibrosis via targeting inflammation, fibrosis, and metabolism.* Commun Biol, 2023. **6**(1): p. 1176.
48. Acerbi, I., et al., *Human breast cancer invasion and aggression correlates with ECM stiffening and immune cell infiltration.* Integr Biol (Camb), 2015. **7**(10): p. 1120-34.
49. Nolan, E., G.J. Lindeman, and J.E. Visvader, *Deciphering breast cancer: from biology to the clinic.* Cell, 2023. **186**(8): p. 1708-1728.
50. Barriga, E.H., et al., *Tissue stiffening coordinates morphogenesis by triggering collective cell migration in vivo.* Nature, 2018. **554**(7693): p. 523-527.
51. Zhou, J., et al., *Macroscopic stiffening of embryonic tissues via microtubules, RhoGEF and the assembly of contractile bundles of actomyosin.* Development, 2010. **137**(16): p. 2785-94.
52. Handorf, A.M., et al., *Tissue stiffness dictates development, homeostasis, and disease progression.* Organogenesis, 2015. **11**(1): p. 1-15.
53. Kular, J., et al., *A Negative Regulatory Mechanism Involving 14-3-3zeta Limits Signaling Downstream of ROCK to Regulate Tissue Stiffness in Epidermal Homeostasis.* Dev Cell, 2015. **35**(6): p. 759-74.
54. Rath, N., et al., *Rho Kinase Inhibition by AT13148 Blocks Pancreatic Ductal Adenocarcinoma Invasion and Tumor Growth.* Cancer Res, 2018. **78**(12): p. 3321-3336.
55. Wu, S.Z., et al., *Stromal cell diversity associated with immune evasion in human triple-negative breast cancer.* Embo j, 2020. **39**(19): p. e104063.
56. Cazet, A.S., et al., *Targeting stromal remodeling and cancer stem cell plasticity overcomes chemoresistance in triple negative breast cancer.* Nat Commun, 2018. **9**(1): p. 2897.
57. Papanicolaou, M., et al., *Temporal profiling of the breast tumour microenvironment reveals collagen XII as a driver of metastasis.* Nat Commun, 2022. **13**(1): p. 4587.
58. Wu, S.Z., et al., *A single-cell and spatially resolved atlas of human breast cancers.* Nat Genet, 2021. **53**(9): p. 1334-1347.
59. Timpson, P., et al., *Organotypic collagen I assay: a malleable platform to assess cell behaviour in a 3-dimensional context.* J Vis Exp, 2011(56): p. e3089.
60. Pereira, B.A., et al., *Temporally resolved proteomics identifies nidogen-2 as a cotarget in pancreatic cancer that modulates fibrosis and therapy response.* Sci Adv, 2024. **10**(27): p. eadl1197.
61. Chitty, J.L., et al., *A first-in-class pan-lysyl oxidase inhibitor impairs stromal remodeling and enhances gemcitabine response and survival in pancreatic cancer.* Nat Cancer, 2023. **4**(9): p. 1326-1344.
62. Murphy, K.J., et al., *Intravital imaging technology guides FAK mediated priming in pancreatic cancer precision medicine according to merlin status.* Science Advances, 2021. **7**.
63. Vennin, C., et al., *CAF hierarchy driven by pancreatic cancer cell p53-status creates a pro-metastatic and chemoresistant environment via perlecan.* Nat Commun, 2019. **10**(1): p. 3637.
64. Chambers, C.R., et al., *Targeting the NPY/NPY1R signaling axis in mutant p53-dependent pancreatic cancer impairs metastasis.* Sci Adv, 2025. **11**(11): p. eadq4416.
65. Murphy, K.J., et al., *Cell-derived Matrix Assays to Assess Extracellular Matrix Architecture and Track Cell Movement.* Bio Protoc, 2022. **12**(24).
66. Cukierman, E., et al., *Taking cell-matrix adhesions to the third dimension.* Science, 2001. **294**(5547): p. 1708-12.
67. Floerchinger, A., et al., *Optimizing metastatic-cascade-dependent Rac1 targeting in breast cancer: Guidance using optical window intravital FRET imaging.* Cell Rep, 2021. **36**(11): p. 109689.

1185 68. Follain, G., et al., *Fluids and their mechanics in tumour transit: shaping metastasis.* Nat Rev
1186 Cancer, 2020. **20**(2): p. 107-124.
1187 69. Berndt, J.D., et al., *Rho-kinase and myosin II affect dynamic neural crest cell behaviors during*
1188 *epithelial to mesenchymal transition in vivo.* Dev Biol, 2008. **324**(2): p. 236-44.
1189 70. Stankova, V., N. Tsikolia, and C. Viebahn, *Rho kinase activity controls directional cell*
1190 *movements during primitive streak formation in the rabbit embryo.* Development, 2015.
1191 **142**(1): p. 92-8.
1192 71. Conklin, M.W., et al., *Collagen Alignment as a Predictor of Recurrence after Ductal Carcinoma*
1193 *In Situ.* Cancer Epidemiol Biomarkers Prev, 2018. **27**(2): p. 138-145.
1194 72. Feinberg, T.Y., et al., *Divergent Matrix-Remodeling Strategies Distinguish Developmental from*
1195 *Neoplastic Mammary Epithelial Cell Invasion Programs.* Dev Cell, 2018. **47**(2): p. 145-160.e6.
1196 73. Tozluoğlu, M., et al., *Matrix geometry determines optimal cancer cell migration strategy and*
1197 *modulates response to interventions.* Nat Cell Biol, 2013. **15**(7): p. 751-62.
1198 74. Friedl, P., et al., *Classifying collective cancer cell invasion.* Nat Cell Biol, 2012. **14**(8): p. 777-83.
1199 75. Boudaoud, A., et al., *FibrilTool, an ImageJ plug-in to quantify fibrillar structures in raw*
1200 *microscopy images.* Nat Protoc, 2014. **9**(2): p. 457-63.
1201 76. Dumont, N., et al., *Breast fibroblasts modulate early dissemination, tumorigenesis, and*
1202 *metastasis through alteration of extracellular matrix characteristics.* Neoplasia, 2013. **15**(3):
1203 p. 249-62.
1204 77. Benthani, F.A., et al., *'MCC' protein interacts with E-cadherin and beta-catenin strengthening*
1205 *cell-cell adhesion of HCT116 colon cancer cells.* Oncogene, 2018. **37**(5): p. 663-672.
1206 78. Erami, Z., et al., *Intravital FRAP Imaging using an E-cadherin-GFP Mouse Reveals Disease- and*
1207 *Drug-Dependent Dynamic Regulation of Cell-Cell Junctions in Live Tissue.* Cell Rep, 2016. **14**(1):
1208 p. 152-167.
1209 79. Herrmann, D., et al., *Three-dimensional cancer models mimic cell-matrix interactions in the*
1210 *tumour microenvironment.* Carcinogenesis, 2014. **35**(8): p. 1671-9.
1211 80. Timpson, P., et al., *Spatial regulation of RhoA activity during pancreatic cancer cell invasion*
1212 *driven by mutant p53.* Cancer Res, 2011. **71**(3): p. 747-57.
1213 81. Wang, J., et al., *Discovery of unglycosylated indolocarbazoles as ROCK2 isoform-selective*
1214 *inhibitors for the treatment of breast cancer metastasis.* Eur J Med Chem, 2023. **250**: p.
1215 115181.
1216 82. Weisdorf, D.J., et al., *KD025 for Patients with Chronic Graft-Versus-Host Disease (cGVHD) –*
1217 *Long-Term Follow-up of a Phase 2a Study (KD025-208).* Biology of Blood and Marrow
1218 Transplantation, 2020. **26**(3, Supplement): p. S187-S188.
1219 83. Riento, K. and A.J. Ridley, *Rocks: multifunctional kinases in cell behaviour.* Nat Rev Mol Cell
1220 Biol, 2003. **4**(6): p. 446-56.
1221 84. Deng, Z., et al., *Comprehensive understanding of anchorage-independent survival and its*
1222 *implication in cancer metastasis.* Cell Death Dis, 2021. **12**(7): p. 629.
1223 85. Ying, H., et al., *The Rho kinase inhibitor fasudil inhibits tumor progression in human and rat*
1224 *tumor models.* Mol Cancer Ther, 2006. **5**(9): p. 2158-64.
1225 86. Verma, D., et al., *Interplay between cytoskeletal stresses and cell adaptation under chronic*
1226 *flow.* PLoS One, 2012. **7**(9): p. e44167.
1227 87. Horiuchi, A., et al., *Up-regulation of small GTPases, RhoA and RhoC, is associated with tumor*
1228 *progression in ovarian carcinoma.* Lab Invest, 2003. **83**(6): p. 861-70.
1229 88. Liu, X., et al., *ROCK1 as a potential therapeutic target in osteosarcoma.* J Orthop Res, 2011.
1230 **29**(8): p. 1259-66.
1231 89. Vishnubhotla, R., et al., *ROCK-II mediates colon cancer invasion via regulation of MMP-2 and*
1232 *MMP-13 at the site of invadopodia as revealed by multiphoton imaging.* Lab Invest, 2007.
1233 **87**(11): p. 1149-58.
1234 90. Kamai, T., et al., *Significant association of Rho/ROCK pathway with invasion and metastasis of*
1235 *bladder cancer.* Clin Cancer Res, 2003. **9**(7): p. 2632-41.

1236 91. Wong, C.C., et al., *Rho-kinase 2 is frequently overexpressed in hepatocellular carcinoma and*
1237 *involved in tumor invasion.* Hepatology, 2009. **49**(5): p. 1583-94.
1238 92. Mazloomi, S.M., et al., *Profiling the expression of pro-metastatic genes in association with the*
1239 *clinicopathological features of primary breast cancer.* Cancer Cell Int, 2021. **21**(1): p. 6.
1240 93. Filipe, E.C., et al., *Tumor Biomechanics Alters Metastatic Dissemination of Triple Negative*
1241 *Breast Cancer via Rewiring Fatty Acid Metabolism.* Adv Sci (Weinh), 2024. **11**(23): p. e2307963.
1242 94. Bankhead, P., et al., *QuPath: Open source software for digital pathology image analysis.* Sci
1243 Rep, 2017. **7**(1): p. 16878.
1244 95. Barnes, J.M., J.T. Nauseef, and M.D. Henry, *Resistance to fluid shear stress is a conserved*
1245 *biophysical property of malignant cells.* PLoS One, 2012. **7**(12): p. e50973.
1246 96. Piccinini, F., A. Kiss, and P. Horvath, *CellTracker (not only) for dummies.* Bioinformatics, 2016.
1247 **32**(6): p. 955-7.

1248